Dipl.-Ing. Gregor Klinser

Operando Studies of Charging Processes in Battery Cathodes by Magnetometry and Positron Annihilation

DOCTORAL THESIS

to achieve the university degree of

Doktor der technischen Wissenschaften

submitted to

Graz University of Technology

Supervisor

Univ.-Prof. Dr.rer.nat. Roland Würschum

Institute of Materials Physics

Graz, January 2019

Abstract

Research in the field of modern battery materials demands characterization techniques which allow an inspection of atomistic processes during battery charging and discharging. Two powerful tools for this purpose are magnetometry and positron-electron annihilation. The magnetic moment serves as highly sensitive fingerprint for the oxidation state of the transition metal ions, thus enabling to identify the electrochemical "active" ions. The positron lifetime on the other hand, is sensitive to open volume defects of the size of a few missing atoms down to single vacancies providing an unique insight into lattice defects induced by charging and discharging. These aspects in combination with suitable operando techniques open up a new pathway for battery research. Steps in this direction were achieved in the present thesis with the development and application of electrochemical cells for operando measurements of the magnetic susceptibility within a SQUID magnetometer and positron-electron annihilation during charging and discharging.

Magnetic susceptibility measurements on the application-relevant cathode material $LiNi_{1/3}Mn_{1/3}Co_{1/3}O_2$ and the promising Ni rich cathode material $LiNi_{0.6}Mn_{0.2}Co_{0.2}O_2$ during repetitive cycles identified in both cases Ni-, Co- and O-ions as electrochemical active ions. In the case of $Li_xNi_{1/3}Mn_{1/3}Co_{1/3}O_2$ a sequence of oxidation steps from first Ni^{2+} to Ni^{3+} ($1 \geq x > 2/3$), than Ni^{3+} to Ni^{4+} ($2/3 > x > 1/3$), followed by a simultaneously oxidation of Co^{3+}- and O^{2-}-ions ($x < 1/3$) was observed. The charge compensation process of $Li_xNi_{0.6}Mn_{0.2}Co_{0.2}O_2$ could also be divided into three steps. First by a simultaneous oxidation of Ni^{2+} and Co^{2+} ($1 \geq x > 0.53$), followed by a sole Ni^{3+} oxidation ($0.53 > x > 0.21$), and finally by a contribution of Ni^{3+} and Co^{3+} or by Co^{3+} and O^{2-} ($x < 0.21$).

The potential of the developed operando cell for magnetic susceptibility measurements is demonstrated not only for Li-ion batteries but also for post-Li batteries using

as an example the attractive Li-ion alternative, $Na_xV_2(PO_4)_3$. First measurements of this kind revealed the charge compensation process to be entirely due to $V^{3+} \leftrightarrow V^{4+}$ oxidation/reduction during charging/discharging. However, during the first battery cycle the change in magnetic susceptibility indicates additional processes not contributing to battery charging, which can not be seen from electrochemical measurements.

The charging induced lattice defects in $Li_xNi_{1/3}Mn_{1/3}Co_{1/3}O_2$ have been found to be dominated by Li-ion mono vacancy, di-vacancies and vacancy agglomerates formation. Moreover, indications for a structural phase transition and vacancy reordering processes at certain Li contents have been found.

These results impressively demonstrate the capability of operando magnetic and positron-annihilation measurements for battery research and development.

Kurzfassung

Für die Entwicklung und Erforschung von Batteriekathoden werden Charakterisierungsmethoden benötigt, die einen Einblick in atomare Prozesse während des Be- und Entladens gewähren können. Zwei dafür geeignete Methoden stellen die Magnetometrie sowie die Positron-Elektron Annihilation dar. So können über die magnetischen Momente der Übergangsmetallionen, die sehr empfindlich von deren Oxidationsstufen abhängen, die für die Ladungsneutralität verantwortlichen Ionen identifiziert werden. Die bei der Be- und Entladung entstehenden Gitterdefekte lassen sich durch Messung der Positronenlebensdauer bestimmen. Dabei wird ausgenützt, dass die Positronenlebensdauer ein spezifisches Maß für die Größe von freiem Volumen im Bereich eines einzigen bis hin zu einigen wenigen fehlenden Atome ist. Durch Kombination der Positron-Elektron Annihilation/Magnetometrie mit operando Messmethoden, haben sich neue Möglichkeiten zur Charakterisierung atomarer Prozesse in Batteriekathoden ergeben. Im Rahmen dieser Dissertation wurden elektrochemische Zellen für magnetische Suszeptibilitätsmessungen in einem SQUID Magnetometer sowie für die Positronen-Elektronen Annihilationsmessung, während des Be- und Entladens einer Batteriekathode, entwickelt.

Die magnetischen Suszeptibilitätsmessungen an den anwendungsrelevanten Kathodenmaterialien $LiNi_{1/3}Mn_{1/3}Co_{1/3}O_2$ und den vielversprechenden Ni reicheren Kathodenmaterial $LiNi_{0.6}Mn_{0.2}Co_{0.2}O_2$ über mehrere Ladezyklen, haben in beiden Fällen Ni-, Co- und O-Ionen als elektrochemisch aktive Ionen identifiziert. Im Fall von $Li_xNi_{1/3}Mn_{1/3}Co_{1/3}O_2$ wurden aufeinanderfolgende Oxidationsprozesse von Ni^{2+} zu Ni^{3+} ($1 \geq x > 2/3$), von Ni^{3+} zu Ni^{4+} ($2/3 > x > 1/3$) sowie von einer simultanen Oxidation von Co^{3+}- und O^{2-}-Ionen ($x < 1/3$) gefunden. Für das Kathodenmaterial $Li_xNi_{0.6}Mn_{0.2}Co_{0.2}O_2$ konnten ebenfalls drei unterschiedliche Bereiche ausgemacht werden. Eine simultane Oxidation von Ni^{2+} und Co^{2+} ($1 \geq x > 0.53$), gefolgt von

einer reinen Ni^{3+} Oxidation ($0.53 > x > 0.21$) und schlussendlich einer gleichzeitigen Oxidation von Ni^{3+} und Co^{3+} oder von Co^{3+} und O^{2-} ($x < 0.21$).

Das Potential der entwickelten operando Zelle für Messungen der magnetische Suszeptibilität konnte nicht nur für Li-Ionen Batteriematerialien sondern auch für post-Li Batterien am Beispiel des attraktiven Kathodenmaterials, $Na_xV_2(PO_4)_3$ aufgezeigt werden. Erste Messungen dieser Art haben für die Ladungsneutralität ausschließlich $V^{3+} \leftrightarrow V^{4+}$ Oxidations/Reduktionsprozesse während des Be/Entladens gezeigt. Das weitern deuten die magnetischen Messungen auf irreversible elektrochemische Prozesse im ersten Ladezyklus hin.

Mit Hilfe der Positronenlebensdauer Messungen an $Li_xNi_{1/3}Mn_{1/3}Co_{1/3}O_2$ konnte gezeigt werde, dass mit zunehmender Beladung neben Einfachleerstellen auch Doppelleerstellen und Leerstellenclustern gebildet werden. Unter anderem wurden dabei auch Hinweise dafür gefunden, dass sich Leerstellencluster bei hoher Li-Extraktion in kettenförmige Cluster umordnen.

Anhand dieser Ergebnisse kann eindrucksvoll das Potential von Operando-Messungen für die Batterieforschung und Entwicklung gezeigt werden.

Contents

CHAPTER 1

Introduction

Li-ion batteries have developed into the most advanced battery systems. Depending on the area of application different cathode materials are used. $LiCoO_2$ for example has developed as the cathode material of choice for consumer electronics like notebooks or cell phones. The increasing demands for energy storage devises, like for electric vehicles or stationary applications, however, requires cathode materials with reduced cost and increased energy density. Substituting Ni for Co, $LiNiO_2$, would emerge as an attractive cathode material to fulfill these requirements [1, 2]. Despite the high capacity there are safety issues with $LiNiO_2$ and difficulties in synthesis as Ni atoms tend to end up in the Li sublattice hindering the Li diffusion [3]. While the synthesis issues can be overcome by only partially substituting Co by Ni, the safety issue is solved by adding Mn to this compound. As Co is expensive and Mn electrochemical inactive in $LiNi_xMn_yCo_zO_2$ tremendous research effort is undertaken to increase the Ni content. $LiNi_{1/3}Mn_{1/3}Co_{1/3}O_2$ and $LiNi_{0.5}Mn_{0.3}Co_{0.2}O_2$ are already commercialized cathode materials. Cathode materials with higher Ni content like $LiNi_{0.6}Mn_{0.2}Co_{0.2}O_2$ and $LiNi_{0.8}Mn_{0.1}Co_{0.1}O_2$ are also very promising. However, these Ni rich cathodes often suffer for capacity loss within the first few cycles which has a negative impact not only on the maximum capacity but also on the cycle life [4, 5].

The fast crowing field of stationary battery storage applications increase the pressure on the lithium price due to the distribution and accessibility of the Li ore deposits [6]. For this reason, beside the development of Ni-rich cathode materials also tremendous effort are undertaken to develop post lithium ion cathode materials. One material class having high potential in this field are sodium ion batteries, see e.g. [7–9]. On the one hand, a easy supply of sodium does not increase the costs. On the other hand,

the similarities to Li-ions allows to use similar or even identical host structures and, thus, a fast development can profit by mimicking what is already known for Li-ion battery cathodes [8]. Nevertheless, the large ion radius of sodium results in lower energy densities and increased weight of these batteries such that they are primarily considered for stationary application rather than to replace Li-ion cathode materials in portable electronics [8, 9].

This increasing demand in terms of quality and progress in the field of batteries requires understanding and optimization of the variety of complex electrochemical and physical processes, such as oxidation/reduction processes, phase transitions, volume changes, defect formation, side reactions, etc. occurring during battery cycling. Within this thesis two of these issues are addressed:

- Defect formation: Defects play a major role for diffusion and structural stability of cathode materials, thus, they are of utmost interest not only in new cathode materials but also in well established materials, e.g., a structural change occurs in Li_xCoO_2 cathode materials when the Li content x drops below 0.5, which drastically reduces the capacity [10–15]. Currently, structure-sensitive in-situ and operando techniques, like X-ray diffraction, scanning probe techniques, electron microscopy, or magnetometry are available for studying various kind of defects during battery cycling, see for example [16–19]. It seems obvious that for this kind of studies also the highly defect-specific technique of positron−electron annihilation could give very valuable contributions to charging induced defect on the Li-sublattice. This especially refers to the sensitivity of positrons to defects ranges of the size as low as a single missing atom up to voids with diameters of several nanometers. The capability of positron annihilation spectroscopy to battery cathode materials have already been proven by ex-situ measurements, see for example P. Parz *et al.* [20] or S. Seidlmayer *et al.* [21].

- Oxidation/reduction processes: The role of transition metal ions in battery cathodes is often not fully understood, especially when their positive effect to the cathode performance is found by empirical methods. However, improving existing cathode materials and developing new materials demands for a clear understanding and identification of the ions undergoing oxidation/reduction process as well as their reversibility upon battery charging and discharging. For this purpose numerous characterization techniques, like-ray photoelectron spectroscopy [22], X-ray absorption spectroscopy [23–33], nuclear magnetic resonance

spectroscopy [33], electron paramagnetic resonance spectroscopy [34–36], electron energy loss spectroscopy [37], or theoretical calculations [30, 38] are available[1]. Another potential measurement technique is magnetometry [31, 34, 36, 39], as the magnetic properties of cathode materials are highly sensitive to the oxidation state of the transition metal ions; the magnetic moment serves as a fingerprint for these oxidation states.

At first sight, studying these two issues seems like an easy task. However, one challenge in the field of batteries is the fact that during operation different processes often occur simultaneously and, thus, an accurate allocation of single processes requires monitoring during a state of operation. Another challenge is the preparation and handling of samples for ex-situ measurements, as battery components are usually very sensitive to oxygen and moisture, which can affect the measurements, e.g., oxygen influences cathodes like Li_xCoO_2 [40]. Moreover, detectable variations are often very small and, therefore, hard to distinguish from scattering occurring between different samples. Therefore, a direct and accurate linkage of these processes to the electrochemical response of a battery can be achieved in the best way by in-situ or operando techniques, where the battery is in operation during characterization. In the last few years, a lot effort was put in the development of operando and in-situ techniques for battery characterization, see review [18].

Conducting operando experiments requires special cell designs such that batteries are fully operational under the circumstances imposed by the diagnostic tool. To study the aforementioned questions, i.e., the charge compensation process and the defect evolution process upon battery cycling, two operando cells have been developed in this thesis. On the one hand, a three-electrode electrochemical cell has been developed suitable for positron-electron annihilation measurements during battery cycling. With this a precise determination of charging–induced defects could be achieved. On the other hand, an electrochemical cell for operando measurement of the magnetic susceptibility of Li-ion battery cathodes in a SQUID magnetometer established by S. Topolovec in his PHD thesis [41] was further developed and optimized to enable cycling efficiencies of up to 98%. With the new cell design the magnetic properties during repetitive battery cycle can be studied.

In this thesis first operando measurements of the positron lifetime of the application relevant Li-ion battery cathode material $LiNi_{1/3}Mn_{1/3}Co_{1/3}O_2$ during battery charging

[1]The given references are restricted to the cathode materials studied within this thesis.

and discharging are presented. With the enhanced sensitivity of operando measurements four different stages in the defect formation process during battery charging could be identified. These findings are presented in chapter 4.2.

While operando positron spectroscopy can give valuable insight in the defect formation process, operando magnetic susceptibility measurements deliver information about the sequence of oxidation states of the transition metal ions involved in the charge compensation processes. Such operando magnetic susceptibility measurements performed on $LiNi_{1/3}Mn_{1/3}Co_{1/3}O_2$ within this thesis could unambiguously clarify the controversial discussed sequences in literature [22–39]. For iso-structural cathode materials with increased Ni contents, the sequences itself are often not studied which is mainly owed the unclear initial states. One of these Ni-rich cathodes with an unclear initial state, $LiNi_{0.6}Mn_{0.2}Co_{0.2}O_2$ [42–44], was investigated within the timeframe of this thesis. A combination of ex-situ and operando measurements could identify the initial condition and the sequence of oxidation steps, which, surprisingly, differs from those obtained for $LiNi_{1/3}Mn_{1/3}Co_{1/3}O_2$. The charge compensation process of both cathode materials are presented in chapter 4.1 of this thesis.

At last, first operando magnetic susceptibility measurements on post lithium batteries were performed. With these measurements, on the one hand the capability of the developed operando battery cell also for post lithium batteries was shown. On the other hand, the charge compensation process in the very promising cathode material $Na_3V_2(PO_4)_3$ was determined, which is presented in chapter 4.1.4.

Before dealing with this issues, the basics of positron-electron annihilation and magnetochemistry are briefly summarized in chapter 2. The experimental techniques as well as the design for the particular electrochemical cells for the operando positron lifetime and magnetic susceptibility measurements are described in chapter 3. In chapter 5 the results (presented in chapter 4) are discussed. At the end, a conclusion of the content of this thesis is drawn in chapter 6.

List of publications arising from this thesis

With the timeframe of this thesis parts of the results have been published in the following articles:

- **Continuous monitoring of the bulk oxidation states in $Li_xNi_{1/3}Mn_{1/3}Co_{1/3}O_2$ during charging and discharging**
  G. Klinser, S. Topolovec, H. Kren, S. Koller, W. Goessler, H. Krenn, and R. Würschum
  App. Phys. Lett. **109** (2016) 213901

  Author Contribution: G. Klinser assembled the operando cell, performed the experimental work, conducted the analysis and interpretation of the SQUID measurement data. He wrote the manuscript and edited the final version together with the co-authors. The cathode preparation was performed by H. Kren and S. Koller. S. Topoloevc and H. Krenn supported the SQUID measurements. The project, data analysis and interpretation as well as the writing process was supervised by R. Würschum.

- **Charging processes in the cathode $LiNi_{0.6}Mn_{0.2}Co_{0.2}O_2$ as revealed by operando magnetometry**
  G. Klinser, M. Stückler, H. Kren, S. Koller, W. Goessler, H. Krenn, and R. Würschum
  J. Power Sources **396** (2018) 791

  Author Contribution: G. Klinser assembled the operando cell, performed the experimental work, conducted the analysis and interpretation of parts of the SQUID measurement data. He wrote the manuscript and edited the final version together with the co-authors. The presented ex-situ measurements as well as parts of the cathode preparation, cell assembling, measurement work and data analysis was performed by M. Stückler in the framework of his master thesis under my co-supervision. Parts of the cathode preparation was done by H. Kren and S. Koller. H. Krenn supported the SQUID measurements. The ICP-MS analysis was performed by W. Goessler. The project, data analysis and interpretation as well as the writing process was supervised by R. Würschum.

- **Process Monitoring of Charging/Discharging of Lithium Ion Battery Cathodes by Operando SQUID Magnetometry**
  G. Klinser, S. Topolovec, H. Krenn, and R. Würschum
  Encyclopedia of Interfacial Chemistry, edited by K. Wandelt (Elsevier, Oxford, 2018) 849

  Author Contribution: G. Klinser wrote the encyclopedia article (invited) and edited the final version together with the co-authors. Measurements, data analysis and interpretations presented in this article were performed by G. Klinser and S. Topolovec. H. Krenn supported the SQUID measurements. The data analysis and interpretation of the presented measurements as well as the writing process of this article was supervised by R. Würschum.

- **Operando monitoring of charging-induced defect formation in battery electrodes by positrons**
  G. Klinser, H. Kren, S. Koller, and R. Würschum
  (December 26, 2018 accepted in App. Phys. Lett.)

  Author Contribution: G. Klinser developed the operando cell, did the cell assembling, performed the experimental work, conducted the analysis and interpretation of the positron lifetime data. He wrote the manuscript and edited the final version together with the co-authors. The cathode preparation was performed by H. Kren and S. Koller. The positron source preparation was performed by G. Klinser and R. Würschum. R. Würschum also supervised the project, data analysis and interpretation as well as the writing process.

Publications not related to this thesis

The following first- and co-author publications are not directly related to this thesis, however, have been published or submitted in the timeframe of this thesis:

- **Charging of lithium cobalt oxide battery cathodes studied by means of magnetometry**
  G. Klinser, S. Topolovec, H. Kren, S. Koller, H. Krenn, and R. Würschum
  Solid State Ionics **293** (2016) 64

  Author Contribution: G. Klinser performed the experimental work, conducted the analysis and interpretation of the SQUID measurement data. He wrote the manuscript and edited the final version together with the co-authors. The sample preparation was performed by H. Kren and S. Koller. S. Topoloevc and H. Krenn supported the SQUID measurements. The project, data analysis and interpretation as well as the writing process was supervised by R. Würschum.

- **Precipitation processes in Al–Mg–Si extending down to initial clustering revealed by the complementary techniques of positron lifetime spectroscopy and dilatometry**
  L. Resch*, G. Klinser*, E. Hengge, R. Enzinger, M. Luckabauer, W. Sprengel, and R. Würschum
  J. Mater. Sci. **53** (2018) 14657
  *Both authors contributed equally to this work.

  Author Contribution: G. Klinser and L. Resch prepared all samples, performed the experimental work, conducted the analysis and interpretation of the positron measurements. They wrote the manuscript and edited the final version together with the co-authors. Dilatometry sample preparation, measurements and data analysis was performed by E. Hengge, R. Enzinger and M. Luckabauer. The combined interpretation of dilatometry and positron measurements was performed by all authors. The writing process was supervised by W. Sprengel and R. Würschum.

- **Operando magnetometry on Li_xCoO_2 during charging/discharging**
  S. Topolovec, H. Kren, G. Klinser, S. Koller, H. Krenn, and R. Würschum
  J. Solid State Electr. **20** (2016) 1491

  Author Contribution: G. Klinser performed the experimental work, conducted the analysis and interpretation of the ex-situ SQUID measurement data.

- **Defects and Charging Processes in Li-Ion Battery Cathodes Studied by Operando Magnetometry and Positron Annihilation**
  R. Würschum, S. Topolovec, G. Klinser, W. Sprengel, H. Kren, S. Koller, H. Krenn, C Hugenschmidt, M. Reiner, T. Gigl, F Berkemeier, and M. Fiedler
  Materials Science Forum **879** (2017) 2125

  Author Contribution: G. Klinser performed the experimental work, conducted the analysis and interpretation of the ex-situ SQUID measurement data.

- **In Situ Real-Time Monitoring of Aging Processes in an Aluminum Alloy by High-Precision Dilatometry**
  M. Luckabauer, E. Hengge, G. Klinser, W. Sprengel, and R. Würschum
  Magnesium Technology 2017. The Minerals, Metals & Materials Series, edited by K. Solanki, D. Orlov, A. Singh, and N. Neelameggham (Springer, 2017) 669

  Author Contribution: G. Klinser and E. Hengge prepared and performed the presented hardness measurements.

- **Diffusion-reaction model for positron trapping and annihilation at spherical extended defects and in precipitate-matrix composites**
  R. Würschum, L. Resch, and G. Klinser
  Phys. Rev. B, **97** (2018) 224108

  Author Contribution: The calculation of the positron trapping and annihilation rate in spherical extended defects was performed by R. Würschum. G. Klinser performed the recalculation to approve the obtained results.

- **Lifetime of Positrons in Nanostructured Nonstoichiometric Silver Sulfide $Ag_{2-\delta}S$**
  A. A. Rempel, S. I. Sadovnikov, G. Klinser, and W. Sprengel
  Jetp Lett. **107** (2018) 4

Author Contribution: G. Klinser performed the experimental work and conducted the data analysis of the positron lifetime measurements.

- **Identification of Different Positron Trapping Sites during Artificial Aging of a Commercial Light Weight Alloy**
  L. Resch, G. Klinser, W. Sprengel, and R. Würschum
  (accepted in AIP Conference Proceedings)

  Author Contribution: G. Klinser and L. Resch prepared all samples, performed the experimental work, conducted the analysis of the positron measurements at a fixed temperature. The interpretation of the positron measurements together with temperature dependent measurements (performed by L. Resch) was conducted by all authors.

- **Positron trapping and annihilation at interfaces between matrix and cylindrical or spherical precipitates modeled by diffusion-reaction theory**
  R. Würschum, L. Resch, and G. Klinser
  (accepted in AIP Conference Proceedings)

  Author Contribution: The calculation of the positron trapping and annihilation rate in spherical and cylindrical extended defects was performed by R. Würschum. G. Klinser performed the recalculation to approve the obtained results.

- **Study of point defects in CdTe:Mn crystals by electrical measurements supported by positron lifetime spectroscopy**
  S. Solodin, L. Resch, G. Klinser, W. Sprengel, Ye. Nykoniuk, Z. Zakharuk, O. Panchuk, P. Fochuk and R.B. James
  (submitted to IEEE Xplore)

  Author Contribution: G. Klinser and L. Resch performed the experimental work and conducted the data analysis and interpretation of the positron lifetime measurements.

CHAPTER 2

Basics

In this chapter a brief background of positron annihilation in matter (Section 2.1) and of magneto-chemistry (section 2.2) is given. For a more detailed description the reader is referred to Ref. [45, 46] in the case of positron annihilation and Ref. [47] for magneto-chemistry.

2.1 Positron annihilation in matter

The existence of an antiparticle of the electron having opposite charge and magnetic moment, the so called positron e^+, was first postulated in 1928 by Dirac [48] and later experimentally proven by Anderson [49]. While in vacuum e^+ are stable particles they have a finite lifetime when it comes to interaction with matter, due to positron-electron annihilation. About 3 decades later a strong correlation between positron lifetime and temperature in metals was found which was attributed to the formation of lattice vacancies [50]. From that the so–called technique of positron annihilation spectroscopy for studying free volume defects rapidly developed. In the following a brief overview of the basic principles of positron annihilation will be presented.

Energetic positrons from a radioactive decay injected in condensed matter are slowed down to thermal energies within a few pico-seconds [46, 51], first by inelastic scattering with conduction electrons followed by inelastic phonon scattering [52]. The positron implantation profile $\overline{P}(z)$ is dependent on the sample mass density ρ [g/cm^3] and

the maximum positron energy E_{max} [MeV] and was estimated by Brandt and Paulin to [53]:

$$\overline{P}(z) = \exp(-\alpha z) \qquad \text{with} \qquad \alpha = 17 \times \frac{\rho}{E_{max}^{1.43}}. \tag{2.1}$$

With Eq. (2.1) for the sodium isotope ^{22}Na the fraction of positrons I penetrating a certain distance z can be estimated:

$$I = I_0 \exp(-z/z_0) \tag{2.2}$$

with z_0 the mean implantation depth

$$z_0 = \frac{\rho\,[\mathrm{mg/cm^2}]}{25}. \tag{2.3}$$

Once thermalized, the positron diffuses through the crystal before annihilating with an electron of the surrounding. The mean diffusion length of the positron L_+ depends on the mean positron lifetime $\overline{\tau}$ and the positron diffusion coefficient D_+ [54]

$$L_+ = \sqrt{6 D_+ \overline{\tau}}. \tag{2.4}$$

Due to the rather short lifetime of positrons[1], typical positron diffusion lengths in defect free metals are much smaller than the implantation depth, thus, with energetic positrons from β^+ decay the bulk of the material can be probed.

In the periodic lattice of a defect–free metal positrons are in delocalized states, with their probability density being highest between the ion cores due to Coulomb repulsion. Thus, positrons annihilate in the main with conduction electrons. The annihilation from the delocalized state is predominantly into two collinear emitted γ-rays with 511 keV according to the well known conservation of energy equation $E = m_0 c^2$ with m_0 the rest mass of an electron/positron and c the speed of light. Annihilation by three or one γ-rays can be neglected due to the diminishing probability [56]. The annihilation rate λ, which is the inverse of the positron lifetime τ, is determined by the overlap of $n_+(\mathbf{r})$, the positron, and $n_-(\mathbf{r})$ the electron density function [56]

$$\lambda = \tau^{-1} = \pi r_0^2 c \int n_+(\mathbf{r}) n_-(\mathbf{r}) \gamma(n_-) dr. \tag{2.5}$$

[1] Typical positron lifetimes in defect free metals range from 100 to 300 ps, see for example [55]

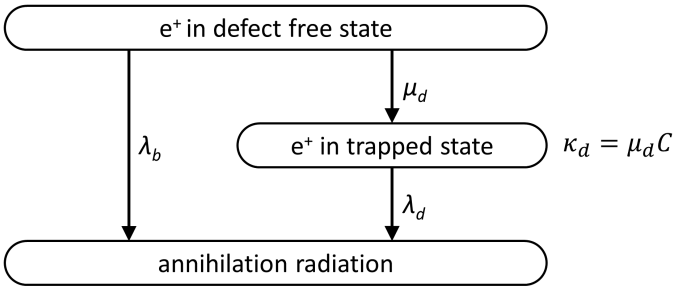

Figure 2.1: Scheme of the trapping model with one particular defect type. Positrons e^+ can either annihilate from a defect free state with the annihilation rate λ_b or get trapped at the defect with the specific trapping rate μ_d (the defect trapping rate κ_d also depends on the defect concentration C) where they annihilate with the rate λ_d.

Here, r_0 is the classical electron radius and $\gamma(n_-)$ describes the enhancement of the electron density in the vicinity of the positron. In the case of simple metals the valance electron density is close to that of a free electron gas and Eq. (2.5) simplifies using the Sommerfeld model to [45]

$$\lambda = \pi r_0^2 c n_-. \tag{2.6}$$

From Eq. (2.6) it is obvious that the positron lifetime in a defect free crystal is material specific as it directly reflects the electron density. The situation changes when crystal defects like vacancies, dislocations, voids, pores or grain boundaries are present as they exhibit additional free volume in the crystal. Due to the absence of positively charged ions[2] positrons experience an attractive potential. As also the electron density is reduced in these sites, positrons trapped at defects will have a lifetime exceeding those of the free state (see Eq. (2.5)). The annihilation characteristics of positrons trapped at defects can be described by transition rate theory [45, 46], which will be outlined in the next section.

2.1.1 Trapping model

Positrons are trapped at defects with the trapping rate κ_d, which can be described by the specific trapping rate μ_d and the defect concentration C

$$\kappa_d = \mu_d C. \tag{2.7}$$

[2]Note: Missing negatively charged ions will result in a repulsion for positrons and, thus, will not be seen.

In the case of one defect type, the temporal evolution of positrons can be described by two dependent rate equations:

$$\begin{aligned} \frac{dn_b(t)}{dt} &= -\lambda_b n_b(t) - \kappa_d n_b(t), \\ \frac{dn_d(t)}{dt} &= \kappa_d n_b(t) - \lambda_d n_d(t). \end{aligned} \tag{2.8}$$

Here, n_b and n_d denote the density of positrons in the free state and in the trapped state, respectively. λ_b and λ_d are the annihilation rates in the defect free state (bulk state) and in the trapped state. The solutions to the differential equations read as

$$\begin{aligned} n_b(t) &= A \exp\left[-\left(\lambda_b + \kappa_d\right) t\right], \\ n_d(t) &= B \exp\left[-\lambda_d t\right] + \tfrac{\kappa_d A}{\lambda_d - (\lambda_b + \kappa_d)} \exp\left[-\left(\lambda_b + \kappa_d\right) t\right]. \end{aligned} \tag{2.9}$$

With the initial condition that at time $t = 0$ all positrons are in the free state, $n_b(0) = 1$ and $n_d(0) = 0$, Eq. (2.9) becomes

$$\begin{aligned} n_b(t) &= \exp\left[-\left(\lambda_b + \kappa_d\right) t\right], \\ n_d(t) &= -\tfrac{\kappa_d}{\lambda_d - (\lambda_b + \kappa_d)} \exp\left[-\lambda_d t\right] + \tfrac{\kappa_d}{\lambda_d - (\lambda_b + \kappa_d)} \exp\left[-\left(\lambda_b + \kappa_d\right) t\right]. \end{aligned} \tag{2.10}$$

And thus, the total number of positrons

$$n(t) = n_b(t) + n_d(t) = I_1 \exp\left[-\frac{t}{\tau_1}\right] + I_2 \exp\left[-\frac{t}{\tau_2}\right] \tag{2.11}$$

with the abbreviations

$$\begin{aligned} I_1 &= 1 - I_2, & \tau_1 &= \frac{1}{\lambda_b + \kappa_d}, \\ I_2 &= \frac{\kappa_d}{\lambda_b - \lambda_d + \kappa_d}, & \tau_2 &= \frac{1}{\lambda_d}. \end{aligned} \tag{2.12}$$

In the experiment, the total annihilation probability is measured which is given by the the absolute value of the time derivative of Eq. (2.11)

$$|P(t)| = \left|\frac{dn(t)}{dt}\right| = \frac{I_1}{\tau_1} \exp\left[-\frac{t}{\tau_1}\right] + \frac{I_2}{\tau_2} \exp\left[-\frac{t}{\tau_2}\right] \tag{2.13}$$

From Eq.(2.13) (case of one defect type) it can be seen that the experimentally observed spectrum consists of two exponential decays. Moreover, together with Eq.(2.12) it is obvious that the intensities I_i as well as the lifetime component τ_1 [3] are depended on

[3] τ_1 is called the reduced bulk lifetime component as τ^{-1} corresponds to the depopulation by annihilation of the free state and by trapping in defects.

the trapping rate κ_d. If κ_d becomes small the defect related intensity I_2 vanishes and the lifetime spectrum becomes single exponential with τ_1 equal to the bulk lifetime τ_b. On the other hand, if κ_d becomes large, I_2 is approximate 1: Saturation trapping occurs, which means that no positrons annihilate from the defect free state or in other words all positrons get trapped in the defect. Using typical values for single vacancies of μ_d[4] (in the range of $10^{14}\,\mathrm{s}^{-1}$ to $10^{15}\,\mathrm{s}^{-1}$ [46, 55]) and the bulk lifetime (in the range of 100 ps [54]), the sensitivity of positron spectroscopy to defect concentration is from 10^{-4} to 10^{-7} [57].

An important variable from which relative changes in defect concentration can be determined is the average positron lifetime $\overline{\tau}$, because $\overline{\tau}$ is in the most cases insensitive to the numerical fitting procedure. The average positron lifetime can be calculated from the lifetime components and their corresponding intensities. In the case of one defect type $\overline{\tau}$ reads

$$\overline{\tau} = \int_0^\infty P(t)dt = \sum_{i=1}^{2} I_i\tau_i = I_1\tau_1 + I_2\tau_2. \tag{2.14}$$

2.2 Magneto-chemistry

The childhood of magneto-chemistry lies in the pioneering works by Michael Faraday. It's development is characterized by the famous scientists Pierre Curie, Paul Langevin, Pierre Weiss, Louis Néel, or John H. Van Vleck, just to name a few of them. In this section a brief outlook of magneto-chemistry [47] with a focus on battery cathodes will be given.

The correlation of magnetization M and the magnetic field H is described by the magnetic susceptibility $\chi = {}^{\partial M}/_{\partial H}$. A material is diamagnetic if the susceptibility is negative $\chi < 0$ resulting in a weakening of the magnetic field inside the material. Although diamagnetism is a feature of all materials it plays a minor roll in magneto-chemistry. More relevant are paramagnetic features arising from isolated centers with unpaired electrons the susceptibility of which increases with decreasing temperature (i.e., enhances the magnetic field inside the material, $\chi > 0$). For low magnetic

[4] It should be noted that μ_d can experimentally only be obtained if the defect concentration is known from other experiments than positron annihilation spectroscopy. Alternatively μ_d can be obtained by theoretical calculations.

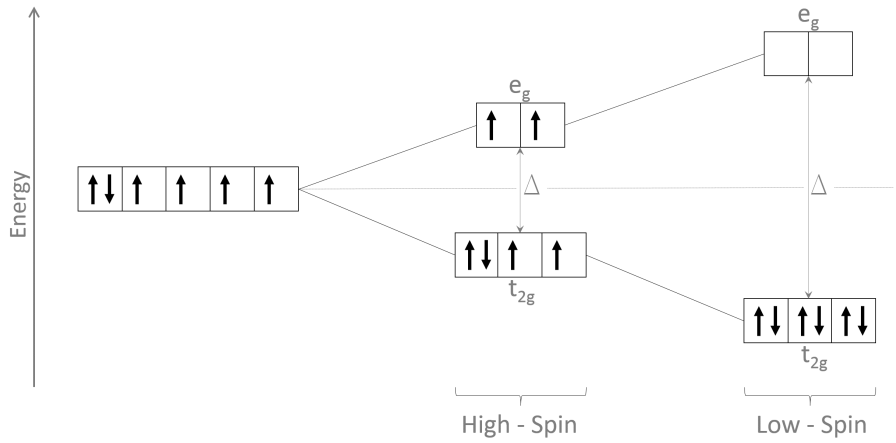

Figure 2.2: Schematic illustration of a $3d^6$-complex (e.g. Co^{3+}) with increasing ligand field splitting Δ from left to right: Free ion (left), high–spin configuration in an intermediate strong ligand field (middle) and low–spin configuration in a strong ligand field reducing the spin multiplicity (right).

fields[5] the temperature dependence of the susceptibility can be described by the Curie law $\chi_{mol} = C/T$ or in the more general case, if magnetic ordering occurs at lower temperatures, by the Curie-Weiss law (above the ordering temperature):

$$\chi_{mol} = \frac{C}{T - \Theta} = \mu_0 \frac{N_A \mu^2}{3k_B(T - \Theta)}. \tag{2.15}$$

Here, C denotes the Curie constant, N_A the Avogadro constant, k_B the Boltzmann constant, T the temperature, Θ the Currie-Weiss temperature, μ_0 the vacuum permeability ($\mu_0 = 1$ in cgs units), and μ the magnetic moment. In the case of free paramagnetic ions with weak spin-orbit interaction the magnetic moment can be derived from the electronic configuration[6] and leads to:

$$\mu = g_J \sqrt{J(J+1)} \mu_B \tag{2.16}$$

with J the total angular momentum quantum number, g_J the Landé g-factor, and μ_B the Bohr magneton.

[5] In the classic derivation by Langevin the temperature variation of the magnetic susceptibility is described by the Langevin function $L(\alpha) = \coth \alpha - 1/\alpha$. For $\alpha \ll 1$ the Langevin function can be approximated by its tangent in the origin (at $\alpha = 0$). This approximation lead to the well known Curie-law. For $B = 0.5\,\mathrm{T}$, $T = 300\,\mathrm{K}$ and $S = 1$ which are typical values within this thesis, $\alpha = 0.04$ and, thus, the condition of $\alpha \ll 1$ is fulfilled.

[6] Note due to the Pauli exclusion principle electrons have to differ at least in one quantum number.

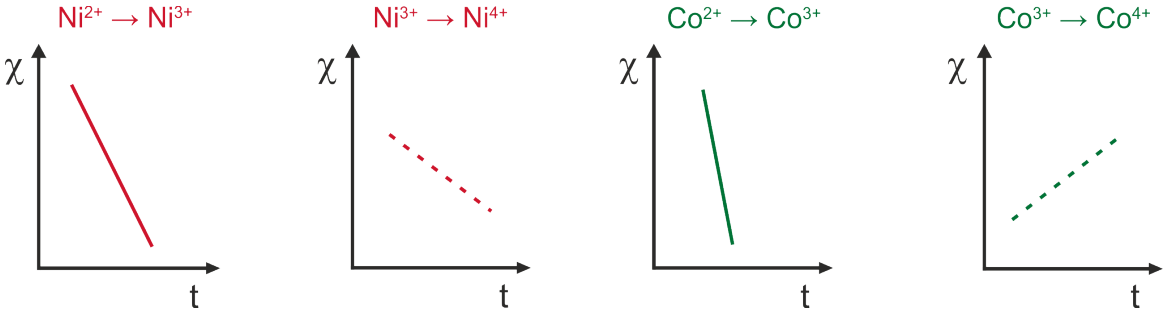

Figure 2.3: Magnetic susceptibility variation upon charging
Schematic drawing of the variation of the magnetic susceptibility χ as a function of charging time t for different oxidation processes of $Ni^{2+}(S = 1) \rightarrow Ni^{3+}$ (S=1/2) (red line), $Ni^{3+}(S = 1/2) \rightarrow Ni^{4+}$ (S=0) (red dashed line), $Co^{2+}(S = 3/2) \rightarrow Co^{3+}$ (S=0) (green line) and $Co^{3+}(S = 0) \rightarrow Co^{4+}$ (S=1/2) (green dashed line). Note: The spin states for the ions where chosen according the relevance for this thesis (see discussion).

However, in battery cathodes the ions are chemically bound, which will lead to deviations from the behavior of free ions. These deviations strongly depend on the interaction of the ions with its surrounding (Ligand field theory). For the 3d-systems the strength and symmetry of the ligand field can lead to a situation where the orbital momentum is partially or even completely suppressed. In the case of octahedral coordinated transition metal oxides, like it is the case for most Li-ion battery cathodes, the ligand field strength can reach values high enough not only to suppress the orbit momentum but even to reduce spin multiplicity compared to the free ion (see Fig. 2.2)[7]. In these cases the magnetic moment in Eq. (2.16) reduces to the spin-only value ($g \approx 2$):

$$\mu = 2\sqrt{S(S+1)}\mu_B. \tag{2.17}$$

As charging/discharging of Li-ion battery cathodes results in the oxidation/reduction of transition metal ions, each of them carrying a different magnetic moment, Eqs. (2.15) and (2.17) can be used to identify the transition metal ion and its oxidation state involved in the charge compensation process. In particular charging/discharging with a constant rate will result in a linear variation of the magnetic susceptibility $\chi(t)$ with time, the slope of which being specific for the oxidation/reduction process (e.g. see Fig. 2.3).

$$\chi_{mol}(t) = \mu_0 \frac{N_A \mu_{eff}(t)^2}{3k_B(T-\Theta)} \qquad \text{with} \qquad \mu_{eff}(t)^2 = \sum c_i(t)\mu_i^2 \tag{2.18}$$

[7] A reduced spin multiplicity is possible if the ligand field effect exceeds the electron-electron interaction.

Here μ_i denotes the effective magnetic moment of the transition metal ions in the respective oxidation state and c_i their concentration ($\sum c_i(t) = 1$).

CHAPTER 3

Experimental Methods

This chapter provides an overview of the experimental methods and set-ups applied in the present study. Section 3.1 deals with the basic principle of the SQUID magnetometer and the corresponding measurement technique and section 3.2 with the positron annihilation spectroscopy. In section 3.1.1 a SQUID-electrochemistry cell designed for magnetic susceptibility measurements and in section 3.2.1 a positron-electrochemistry cell designed for positron annihilation lifetime and Doppler broadening measurements during operando battery charging and discharging are presented. The detailed experimental procedure as well as the sample preparation is outlined in section 3.1.2 and 3.1.3 for the magnetic measurements and in section 3.2.2 for the positron annihilation lifetime measurements.

3.1 SQUID magnetometry

A SQUID (**S**uper Conducting **Q**uantum **I**nterference **D**evices) magnetometer is a sensitive measurement technique to detect relative changes of the magnetic moment of as low as 10^{-8} emu ($1\,\text{emu} = 10^{-3}\,\text{Am}^2$) [58]. The SQUID measurements presented in this thesis were performed in collaboration with Univ.-Prof. Heinz Krenn at the Institute of Physics, University of Graz using a MPMS®-XL-7 magnetometer (Quantum Design Inc.). In the following the measurement principle of this particular SQUID magnetometer will be presented.

As illustrated in Fig. 3.1 a magnetized sample is pulled in discrete steps through superconducting pick-up coils forming a gradiometer of second order. For the present

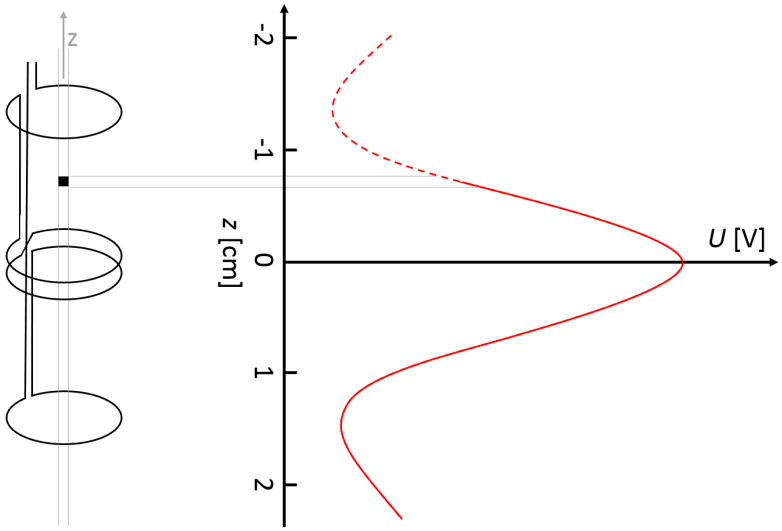

Figure 3.1: Left panel: Schematic drawing of the SQUID pick-up coils forming a second order gradiometer. Right panel: An output voltage U proportional to the magnetic moment is produced by the SQUID sensor as a function of position z.

measurements a scan length of 6 cm with 64 data points per scan were chosen. Such a movement of the sample results in a magnetic flux change $\Phi(z)$ which induces a super-current in the pick-up coils proportional to the magnetic moment of the sample. The induced super-current is inductively coupled to a radio-frequency SQUID sensor, consisting of a superconducting ring with one Josephson junction and a resonant tank circuit. The SQUID sensor produces an output voltage $U(z)$ as function of horizontal position z in the pick-up coils which is proportional to the initial flux-change $\Phi(z)$ (see Fig. 3.1). The magnetic moment is obtained by applying a least square fit to $U(z)$ using the theoretical response function of magnetic point dipole. It should be noted that the approximation of a point dipole is valid as long as the coil radius and the distance between the coils of the gradiometer is large compared to the sample size. In the magnetometer used, with coil distances of 15.19 mm and a coil radius of 9.7 mm, the relative error for a cylindrical sample with the size of 3 mm by 3 mm is less than 1% [58].

3.1.1 Operando SQUID-battery cell

For this thesis an electrochemical cell has been used and further optimized that allows for operando magnetic susceptibility measurements in a SQUID magnetometer. A

first electrochemical SQUID cell was originally designed by T. Traußnig [59] and subsequently improved by S. Topolovec [41], e.g., by installing of a reference electrode. S. Topolovec also modified the electrochemical cell design to study battery cathodes. To obtain sufficient magnetic response, cathodes of several milligrams had to be used [41], which was achieved by increasing the cathode thickness. This led to higher capacity fading as would be expected for commercialized batteries. Within the present thesis, supported by the master thesis of M. Stückler [60] under my supervision, the cell has been substantially improved to reduce this capacity loss and, thus, to increase the reversibility[1]. A schematic drawing of the improved cell design and an exemplary measurement on $LiCoO_2$ can be seen in Fig. 3.2.

The constraints and demands for reliable magnetic measurements and a simultaneous good battery performance are summarized in the following:

(a) The diameter of the cell is limited to $< 9\,\text{mm}$ due to the diameter of the sample space in the SQUID magnetometer. This was realized by using a polyethylene tube with an outer diameter of 5 mm as cell compartment.

(b) For a precise measurement of the magnetic signal the magnetic background should be minimized. This can be achieved by using long homogenous parts which extend well above the pick-up coils or if parts are outside the pick-up coils at any time of the measurement (see measurement principle in chapter 3.1). As it can be seen in Fig. 3.2 the reference electrode of the cell is outside the pickup coils (distance to the pick up coils during measurement $\geq 1.5\,\text{cm}$). The cell compartment as well as the electrolyte stick out of the pick-up coils at any time of the measurement (distance of the end of the compartment to the pick up coils during measurement $\geq 2.5\,\text{cm}$). Neither of these compounds will lead to a flux change. Nevertheless, the separator and the anode contribute to the measured signal. As outlined in chapter 2.2, the quantity of interest, however, is the change of the magnetic susceptibility during battery charging/discharging. As it is obvious, the magnetic signal of the separator does not change. But also the change of the magnetic signal of the Li-anode due to Li deposition and dissolution is negligible small during charging and discharging. This is demonstrated in Fig. 3.3 showing a comparison between the change in magnetic

[1] Not all measurements presented in this thesis have been performed with the improved cell design. Parts have been performed using the cell design by Topolovec and, therefore, showing a higher capacity loss.

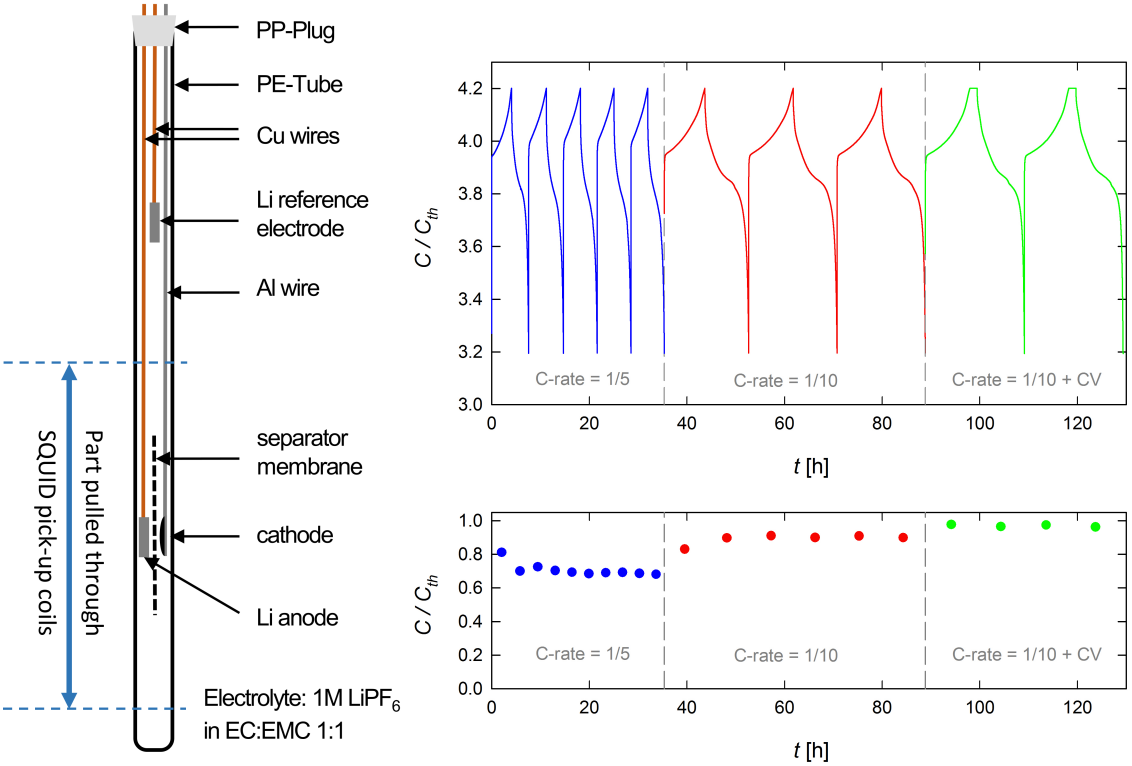

Figure 3.2: Self-developed battery cell for magnetic measurements
Left panel: Schematic drawing of the self-developed operando SQUID magnetometer cell. Note: The part which is pulled through the SQUID pick-up coils is 6 cm long. Upper right panel: Electrode potential U of Li_xCoO_2 cathode as a function of charging time for 10 consecutive cycles of charging/discharging with cut off potentials 4.2 and 3.2 V. Charging was performed with C/5-rate (in blue: cycles 1-5), C/10-rate (in red: cycles 6-8) and C/10-rate where a constant voltage step was applied at the end of charging (in green: cycles 9-10). Lower right panel: nominal weighted capacity c/c_{th} for each charging/discharging cycle. Note: The definition of the C-rate can be found as footnote on page 24.

moment of a battery cell and a reference cell. For the reference measurement Li plating and dissolving was achieved by applying a current between reference electrode and anode.

(c) All parts used must be resistant against the battery electrolyte.

(d) As the cell components are very sensitive to air (oxygen and moisutre), cell assembling and measurements must be possible under protective Ar-atmosphere. Moreover, the battery cells have to be vacuum tight since upon mounting in the SQUID magnetometer the cell has to be transferred through an air-lock that is intermediately evacuated.

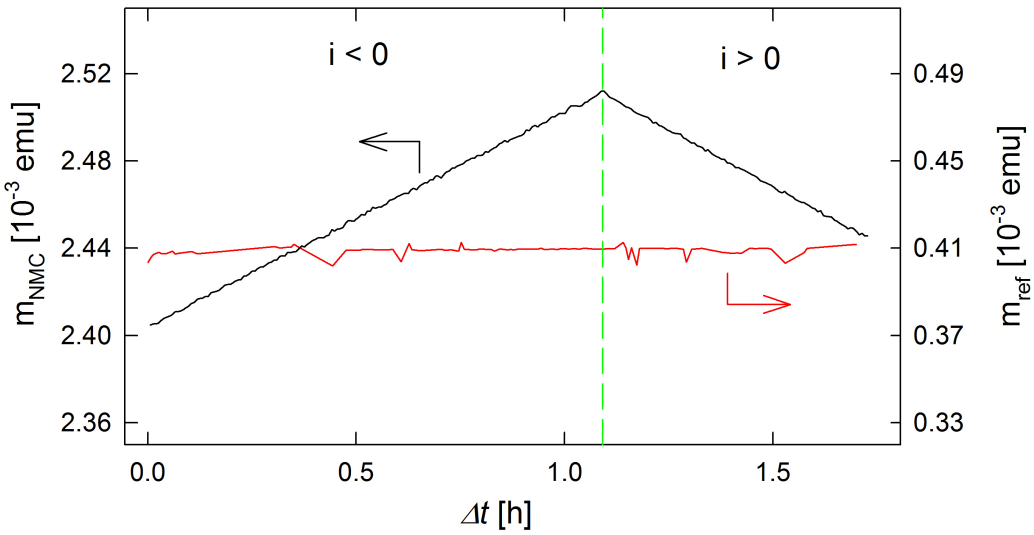

Figure 3.3: Influence of Li-anode
Comparison between the change in magnetic moment m_{NMC} of a operando cell, where $LiNi_{1/3}Mn_{1/3}Co_{1/3}O_2$ was used as cathode material, and the magnetic moment of a reference cell m_{ref} which was apart the missing cathode identically assembled. Li plating/dissolving on the anode side of the reference cell was achieved by applying a current between reference electrode and anode. The chosen current was even 5 times higher as the C/10 current of the battery cell. Note: (i) Scales of left and right y-axes are identical except of a constant offset. (ii) The observed variation of the magnetic moment for the reference cell is due to scattering and not due to Li deposition/dissolving.

(e) The cell design should allow for an easy attachment to the SQUID sample holder.

3.1.2 Sample preparation

Li-ion cathodes

The active materials for this study were commercialized powders provided by VARTA Micro Innovation GmbH (Graz, Austria). Chemical analysis of the two active materials, done by inductive coupled plasma mass spectrometry (ICP-MS: Agilent 7500ce), revealed $Li_{1.03}Ni_{1/3}Mn_{1/3}Co_{1/3}O_2$ and $Li_{0.90}Ni_{0.58}Mn_{0.22}Co_{0.2}O_2$. For easier reading the nominal notions $LiNi_{1/3}Mn_{1/3}Co_{1/3}O_2$ and $LiNi_{0.6}Mn_{0.2}Co_{0.2}O_2$ are used except for the parts in the detailed discussion. Both cathode materials have the α-$NaFeO_2$ type rhombohedral crystal structure (Space Group $R\bar{3}m$) [5, 38, 61, 62].

The cathodes were prepared from an electrode slurry consisting of 88 wt.% active material ($LiNi_{1/3}Mn_{1/3}Co_{1/3}O_2$ and $LiNi_{0.6}Mn_{0.2}Co_{0.2}O_2$ respectively), 7 wt.% carbon black (conducting agent) and 5 wt.% polyvinylidene difluoride hexafluoropropylene

copolymer (binder) dissolved in *N*-Methyl-2-pyrrolidone. The cathode for the magnetic operando measurements were prepared by dip-coating a flattened end of an aluminum wire in the electrode slurry while for the magnetic ex-situ measurements by casting the slurry on a 15 μm thick aluminum foil. In both cases the cathodes were pre-dried at 333 K in air and subsequently dried under vacuum condition ($\approx 10^{-4}$ mbar) at 353 K for 24 h. Finally, the cathodes were pressed (hydrostatic pressure of about 100 MPa) to increase the density of the active material and to ensure a good electrical contact to the aluminum current collector. As anode and reference electrode metallic lithium and as electrolyte 1M $LiPF_6$ in ethylene carbonate (EC) and ethyl methyl carbonate (EMC) with a weight ratio of EC/EMC 1:1 was used for most of the experiment. However, for the preparation of the cathodes for the ex-situ magnetic measurement and also for some operando cells on the $LiNi_{1/3}Mn_{1/3}Co_{1/3}O_2$ cathode material, an electrolyte with different weight ratio (EC/EMC 1:2) and an additional additive of 2wt% vinylene carbonate was used. Varying the electrolyte had no noticeable influence on the operando measurement result. The cell assembling was performed under protective argon atmosphere. Details of operando cell assembling for the magnetic measurements can be found in chapter 3.1.1 and for the operando positron lifetime measurements in chapter 3.2.1.

The cathodes for the ex-situ measurements were mounted in a three electrode Swagelok® T-cell. Li extraction was performed in a Maccor Series 4000 battery tester with a C/200-rate[2]. The charging time for pre-defined Li concentrations was determined using the nominal cathode weight and the theoretical capacitance of the active material. After Li extraction the cathodes were dismantled, rinsed with diethyl carbonate to remove the electrolyte, and finally dried in vacuum (10^{-3} mbar) at 353 K for 24 hours. The dried samples were folded in such a way that they remained fixed in the middle of a 14 cm long polyolefin tube (inner diameter 3.2 mm) only because of friction. The polyolefin tube itself was mounted into an NMR-tube (Wilmad 505-PS-7) which was closed with a polypropylene plug and hermetically sealed with epoxy resin. The tube length was chosen such that the tube extended well beyond the pick-up coils of the magnetometer during the measurement scan. In this way the tube does not contribute to the measured magnetic moment (for more details see chapter 3.1.1).

[2]The C-rate is defined as the reciprocal value of the time (in hours) in order to fully charge or discharge the battery according to the maximum practically achievable capacity. For example, a C/200-rate for $LiNi_{1/3}Mn_{1/3}Co_{1/3}O_2$ means that charging up to 4.2 V should take 200 h.

Na-ion cathode

Except for the cathode, anode, reference electrode and electrolyte used, the sample preparation was identical as aforementioned for the Li-ion cathodes. As active material $Na_3V_2(PO_4)_3$ was used. $Na_3V_2(PO_4)_3$ was synthesized by Roman Zettl (Institute for Chemistry and Technology of Materials, TU Graz) using the same sol-gel route as described for $Li_3V_2(PO_4)_3$ in Ref. [63], accept that Li-ions were substituted by Na- ions. The cathodes were prepared from an electrode slurry consisting of 80 wt.% active material ($Na_3V_2(PO_4)_3$) and 10 wt.% carbon black (conducting agent) and 10 wt.% polyvinylidene difluoride hexafluoropropylene copolymer (binder) dissolved in N-Methyl-2-pyrrolidone. As anode and reference electrode metallic sodium and as electrolyte 1M $NaPF_6$ in ethylene carbonate (EC) and propylene carbonate (PC) with a weight ratio of EC/PC 1:1 was used.

3.1.3 Measurement procedure

For the operando magnetic measurements the battery cell was mounted on a modified SQUID sample rod with electrical feed-throughs to enable a connection to the potentiostat (Autolab PGSTAT128N). Charging and discharging was performed with a C/10-rate which is based on the nominal cathode weight and capacitance of 145 mAh/g for $LiNi_{1/3}Mn_{1/3}Co_{1/3}O_2$ and 170 mAh/g for $LiNi_{0.6}Mn_{0.2}Co_{0.2}O_2$, respectively. The operando magnetic measurements were performed at an applied magnetic field of 5000 Oe and a temperature of 300 K. Although both the magnetic signals of cathode and anode are detected, charging/discharging-induced variations of the magnetic susceptibility can entirely be attributed to the cathode because Li plating/dissolving on the anode contributes less than 1% to the overall change of χ (see Fig. 3.3). Note, as only the change of the magnetic signal is of interest (see chapter 2.2) the magnetic signal arising from the PVDF binder and the carbon black has no influence since the signal is about a factor 30 smaller than that of the active material [64].

The ex-situ magnetic susceptibility measurements were performed in field-cooling mode between 300 K and 8 K at a constant magnetic field of of 5000 Oe. In order to subtract the magnetic signals caused by the aluminum substrate and the additives (carbon black and polymer binder), the temperature-dependent susceptibility was measured for both the plain Al substrate and the Al substrate coated with polymer binder and carbon in the same volume ratio as for the samples. By means of these magnetic data along with

the molar weights of all components, a precise correction of the background signal of each sample could be achieved (a detailed description can be found in Ref. [64]).

3.2 Positron annihilation spectroscopy

Positron annihilation spectroscopy consists of two predominantly applied measurement principles, i.e., positron lifetime spectroscopy and Doppler broadening of the annihilation line. Due to the relevance to this thesis in the following only the basics of the principle of positron lifetime measurement are discussed. For positron Doppler broadening measurements the reader is referred to Ref. [45, 46].

In the framework of laboratory measurements ^{22}Na is the most common isotope used as positron sources due to its high positron yield of 90% and the rather long half life of 2.6 years. The decay scheme of ^{22}Na is illustrated in Fig. 3.4. The main advantage of ^{22}Na is the emission of a 1275 keV γ-quantum 3.7 ps after the emission of the positron. This is essential for positron lifetime measurements as it marks the "birth" of the positron; the 1275 keV γ-quantum is, therefore, often called the start quantum. The positron annihilating with an electron results into the emission of two collinear 511 keV γ-quants (see chapter 2.1) which serve as the stop quantum. With a positron annihilation lifetime spectrometer, which will be explained in the following, the time difference between those events can be measured.

To ensure the correct assignment of the correlated start and stop quanta, a positron source with an activity < 1 MBq is chosen. With such a low activity on average there is only a single positron present at any time[3].

To detect the start- and stop quantum a fast-fast positron lifetime spectrometer was used. The block diagram can be seen in Fig. 3.5. At first, with the help of scintillator crystals and photomultiplier tubes (PM), the start/stop quantum is converted to an electrical pulse the intensity of which is proportional to the γ-quantum energy. This pulse is forwarded to the constant fraction differential discriminators (CFDD), which deliver a timing pulse at the arrival time of the input signal irrespective of its height if it is in a certain energy range corresponding to either start or stop signal. A time to amplitude converter (TAC) subsequently generates an output voltage proportional

[3] An activity of 1 MBq corresponds to one positron every μs which exceeds typical positron lifetimes by more than three orders of magnitude.

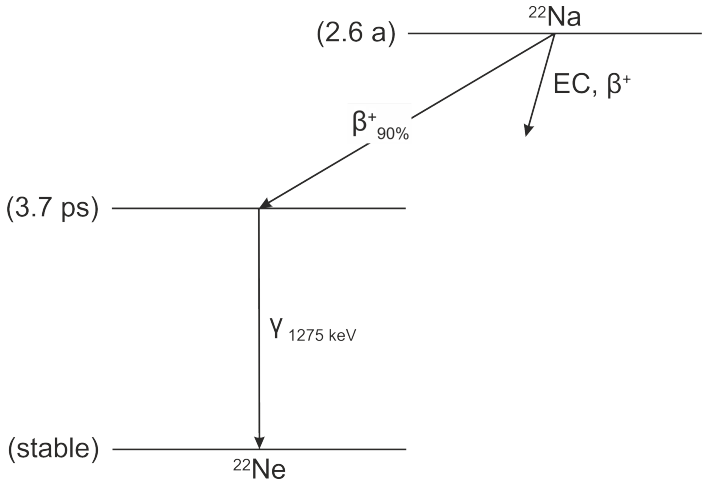

Figure 3.4: Decay scheme of ^{22}Na

to the time difference between the arrival of the start and stop quantum. The stop signal is often delayed before the TAC to ensure that the optimal working range of the TAC can be used.[4] In a last step these output voltages are stored in the multichannel analyzer. Using an analogue-digital converter (not shown in Fig. 3.5) the stored spectrum is transferred to a computer where it can be mathematically analyzed (For the analysis within this thesis the PALS*fit3* program was used [65]). The measured positron lifetime spectrum consists of a sum of exponential decays convoluted with the spectrometer time resolution function and a superimposed background. To extract the positron lifetimes the time resolution function has to be determined in advance. This is possible by measuring ^{207}Bi which emits two γ-quanta separated by 130 ps and which are about in the same energy regions as start and stop quantum [57] or by measuring a defect free sample with known lifetime, like float-zone (FZ) grown silicon. In the present case FZ silicon, well annealed aluminum and copper were used fitting the time resolution function by a sum of three mutually time-shifted Gaussians with different intensities.

As positron source ^{22}NaCl was used encapsulated in two layers of thin hostaphan foil (see next subsection). Thus data analysis also accounted for positrons annihilating within the hostaphan foil ($\tau_{1,Hostaphan} \approx 1800$ ps, $\tau_{2,Hostaphan} \approx 356$ ps and $\tau_{3,Hostaphan} \approx 197$ ps [67]) and the dried NaCl-solution ($\tau_{NaCl} = 420$ ps [68, 69]).

[4] This has no influence on the obtained positron lifetime spectra as only the variation of the time differences is of interested (see chapter 2.1.1)

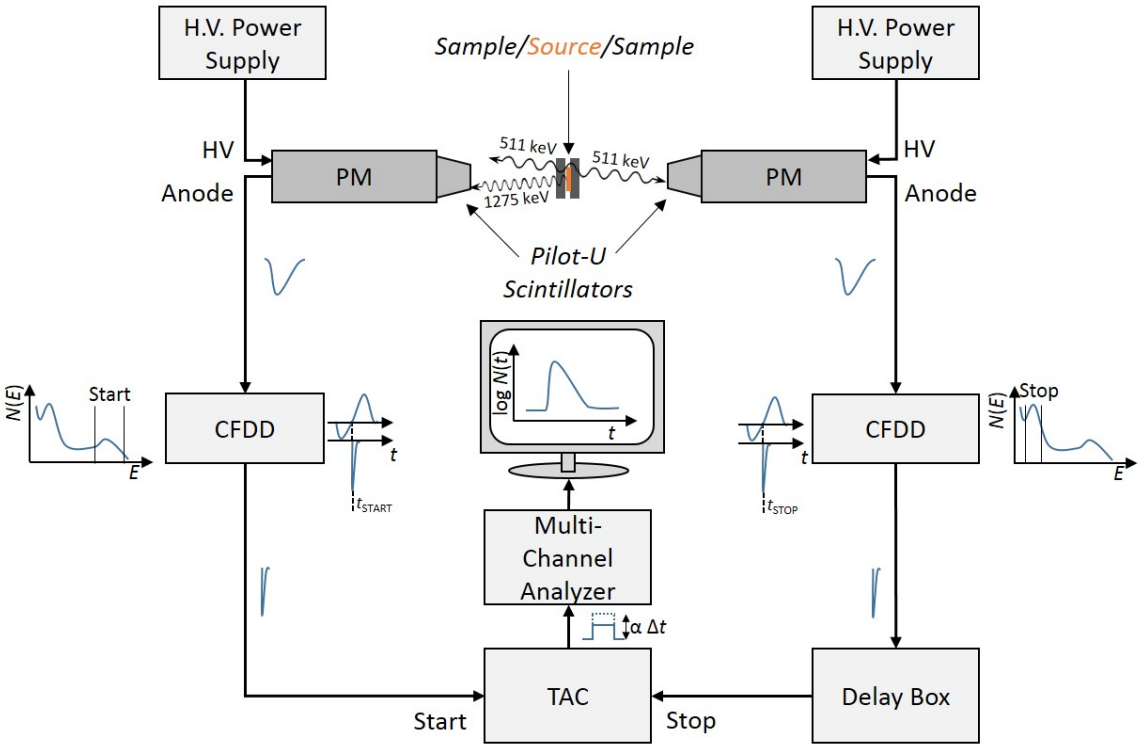

Figure 3.5: Block diagramm of a fast-fast positron lifetime spectrum (redrawn after [66])
H.V. Power Supply ..... Canberra 3002D
PM ..... Hamamatsu photomultiplier tubes H2431-50
CFDD ..... Constant fraction differential discriminator, ORTEC 583B
TAC ..... Time-to-amplitude converter, ORTEC 566
Multichannel analyzer ..... Canberra Multiport II

3.2.1 Operando Positron-battery cell

During this thesis a battery cell suitable for operando positron annihilation spectroscopy was developed which for the first time allows the measurement of the positron lifetime under full electrochemical control: A schematic drawing of the developed cell is illustrated in Fig. 3.6. The developed cell meets the following constraints and demands in order to obtain a good battery performance and simultaneous reliable positron lifetime measurement:

(a) A good cyclability requires that anode and cathode face each other and be as close together as possible, ideally only separated by the separator. Thus, positrons have to be injected through the back side of the cathode material (see Fig. 3.6).

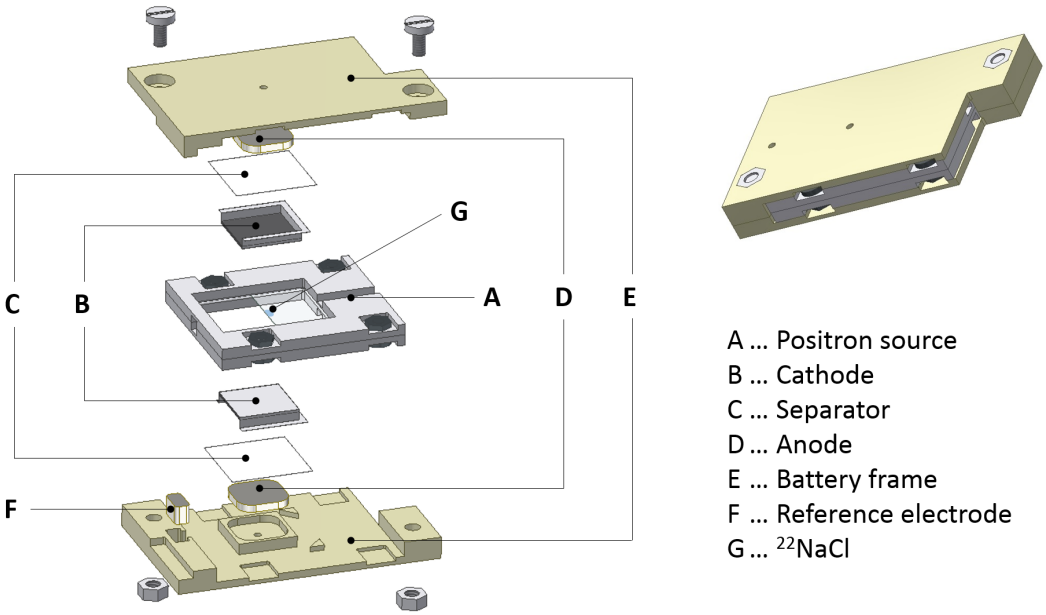

Figure 3.6: Schematic drawing of the battery cell suitable for positron lifetime measurements during battery charging and discharging.

(b) For reliable electrochemical measurements a reference electrode (3-electrode set-up) is included in the cell.

(c) All materials used in the cell design must be stable against the electrolyte. This in particular applies for the positron source to avoid any contamination. Therefore, the ^{22}NaCl was placed between two layers of 15 μm hostaphan foil which are clamped between to Al frames. In addition, all areas where electrolyte might penetrate or diffuse between the hostaphan foils were sealed with epoxy resin.

(d) To increase the maximum number of positrons reaching the active material a sandwich arrangement is required. Therefore, a battery on each side of the positron source is built in the current cell design.

(e) The positron source must be placed within tens of μm to maximize the solid angle of the cathode with respect to the source and to minimize the thickness of the electrolyte layer, the positrons must penetrate before entering the cathode.

(f) Cell assembling and measurement must be possible under protective Ar-atmosphere as battery components are very sensitive to moisture and oxygen. The battery cell shown in Fig. 3.6 is mounted in a specially developed housing with electrical

feedthroughs for a connection to the potentiostat. The housing is filled with electrolyte and sealed against ambient atmosphere.

(g) To guarantee a high detection rate of annihilation events, the photomultiplier tubes should be very close to the battery cell (capture a large solid angle). The current cell design allows to place the start and stop photomultiplier 8 mm apart.

3.2.2 Sample preparation and measurement procedure

The $LiNi_{1/3}Mn_{1/3}Co_{1/3}O_2$ cathodes for the positron measurement were identically prepared as the cathodes for the magnetic ex-situ measurements described in section 3.1.2. Also the anode, reference electrode and electrolyte were identically chosen as for the magnetic measurements.

For the operando positron lifetime measurement the cathodes were mounted in the self developed measurement cell (see chapter 3.2.1) enabling an electrical connection to the potentiostat (Autolab PGSTAT128N). Charging and discharging was performed with a C/50- or C/100-rate which is based on the nominal cathode weight and capacitance of 145 mAh/g for $LiNi_{1/3}Mn_{1/3}Co_{1/3}O_2$. The positron lifetime was measured at room temperature with a positron lifetime spectrometer with a time resolution of 220 ps (FWHM, full width at half maximum) and a count rate of >75 per second. Each analyzed spectra contained about 10^6 annihilation events and were analyzed using the PALS*fit3* program [65]. Positrons annihilating within the source encapsulation, the hostaphan foil (about 7%), and the aluminum current collector (about 14%) are taken into account during data analysis. However, positrons annihilating within the polymer binder, carbon black, and electrolyte contribute to the measured source-corrected spectra such that the absolute value of the positron lifetimes are shifted. As these components can safely be assumed to be constant, any variation of the positron lifetime can be considered to arise from variations within the active material only.

CHAPTER 4

Experimental Results

The experimental results chapter is organized in two parts. First, in section 4.1, the magnetic susceptibility measurements of $Li_xNi_{1/3}Mn_{1/3}Co_{1/3}O_2$ (section 4.1.1), $Li_xNi_{0.6}Mn_{0.2}Co_{0.2}O_2$ (section 4.1.2) and $Na_xV_2(PO_4)_3$ (section 4.1.4) are presented. Results on complementary ex-situ measurements are given in section 4.1.3. In the second part (section 4.2) the defect evolution process is addressed.

Parts of the content presented in section 4.1.1 and 4.1.2 have already been published and are partially reprinted from [G. Klinser, S. Toplovec, H. Kren, S. Koller, W. Goessler, H. Krenn and R. Würschum, Appl. Phys. Lett. **109** (2016) 213901], with the permission of AIP Publishing (section 4.1.1) and from [G. Klinser, M. Stückler, H. Kren, S. Koller, W. Goessler, H. Krenn and R. Würschum, J. Power Sources **396** (2018) 791] (section 4.1.2). Also parts of the content presented in section 4.2 have recently been accepted by Applied Physics Letters.

4.1 Charge compensation process

In the following a detailed description of the measurement results for $Li_xNi_{1/3}Mn_{1/3}Co_{1/3}O_2$ (section 4.1.1) and $Li_xNi_{0.6}Mn_{0.2}Co_{0.2}O_2$ (section 4.1.2) are presented. For both cathode materials the magnetic susceptibility χ was measured during consecutive charging (Li extraction)/discharging (Li insertion) cycles. The samples were mounted under open circuit conditions under which χ remained constant. As can be seen in Fig. 4.1 for $Li_xNi_{1/3}Mn_{1/3}Co_{1/3}O_2$ with the onset of charging χ immediately starts to decrease. For the subsequent cycles, cut-off potentials of 3.2 V for discharging as

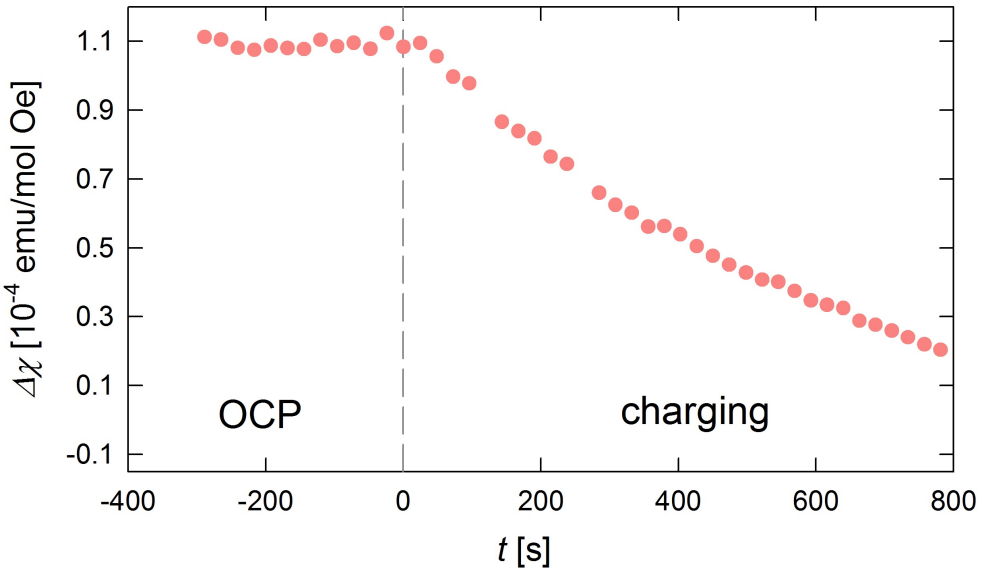

Figure 4.1: Magnetic susceptibility variation under open circuit conditions
Change in magnetic susceptibility $\Delta\chi$ of the $Li_xNi_{1/3}Mn_{1/3}Co_{1/3}O_2$ cathode as a function of time t under open circuit conditions (OCP) and for the first 800 seconds of the subsequent charging cycle. (Corresponding to the initial part (leftmark) in Fig. 4.2)

well as 4.2 V or 4.8 V for charging are chosen. The cut-off potential 4.2 V (in the following referenced as low-potential region) refers to the cut-off potentials used in commercialized Li-ion batteries. In this case, however, for $Li_xNi_{1/3}Mn_{1/3}Co_{1/3}O_2$ the Li contents varies only in a range of $1 \geq x > 0.46$ and for $Li_xNi_{0.6}Mn_{0.2}Co_{0.2}O_2$ in the range of $1 \geq x > 0.29$. In order to study the entire Li concentration regime also measurements with an increased cut-off potential of 4.8 V (in the following referenced as high-potential region) were performed.

4.1.1 $Li_xNi_{1/3}Mn_{1/3}Co_{1/3}O_2$

In Fig. 4.2 the electrode potential U as well as the change in magnetic susceptibility $\Delta\chi$ as a function of charging time t for four repetitive cycles are shown. For the first three cycles the cut off potentials were set to 4.2 V (charging) and 3.2 V (discharging). In the 4^{th} cycle the charging cut off potential was increased to 4.8 V in order study the lower Li concentration region. The observed voltage curves agree with the expected charging and discharging curves. Nevertheless, the capacity loss is higher than what is usually expected for these cathodes. The main reason for this are the rather thick electrodes ($\approx 600\mu$m), the electrode geometry and the charging profile used for this measurements.

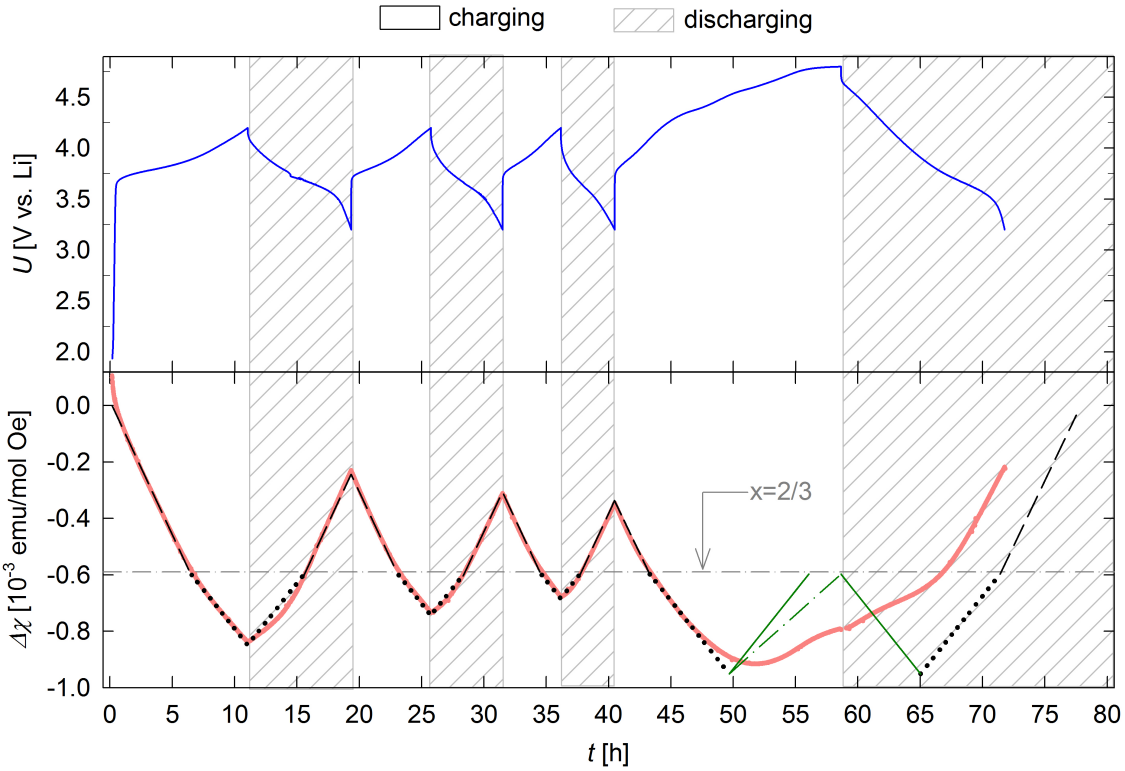

Figure 4.2: Magnetic susceptibility measurements of $Li_xNi_{1/3}Mn_{1/3}Co_{1/3}O_2$
Change in magnetic susceptibility $\Delta\chi$ (red line) and electrode potential U (blue line) of the $Li_xNi_{1/3}Mn_{1/3}Co_{1/3}O_2$ cathode as a function of time t for four consecutive cycles of charging/discharging with cut off potentials 4.2 and 3.2 V (cycles one to three) and an increased upper cut off potential of 4.8 V (4^{th} cycle). The straight lines represent the redox processes for $Ni^{2+}(S = 1) \rightarrow Ni^{3+}$ (S=1/2) (black dashed lines), $Ni^{3+}(S = 1/2) \rightarrow Ni^{4+}$ (S=0) (black dotted lines), and $Co^{3+}(S = 0) \rightarrow Co^{4+}$ (S=1/2) (green lines) according to Eq. (2.18). The green dashed-dotted line represents the corrected slope due to electrolyte oxidation process by assuming complete Li extraction for the end of the charging cycle. The horizontal gray dash-dotted line indicates the Li content of $x = 2/3$.

As can be seen in Fig. 4.2 for the first 30 minutes of charging, a strong decrease of χ occurs, followed by a linear decrease up to $t = 5$ h and a subsequent reduction of the decrease, which merges at $t = 6.9$ h in a reduced linear decrease for about 4.0 h until the end of the first charging cycle is reached (total charging time 10.9 h). In the corresponding fashion, a χ-increase instantaneously sets in with discharging (insertion of Li), at first with a continuously increasing rate between $t = 10.9$ h and 13.6 h and subsequently with a constant rate till the end of the discharging cycle at $t = 19.2$ h (Fig. 4.2). For the subsequent two charging/discharging cycles, the χ-variation is qualitatively the same, apart from the missing initial strong decrease upon charging. At the beginning of the 4^{th} charging cycle, again, the same χ-variation as described above is observed; at first a linear decrease of χ followed by linear decrease with reduced

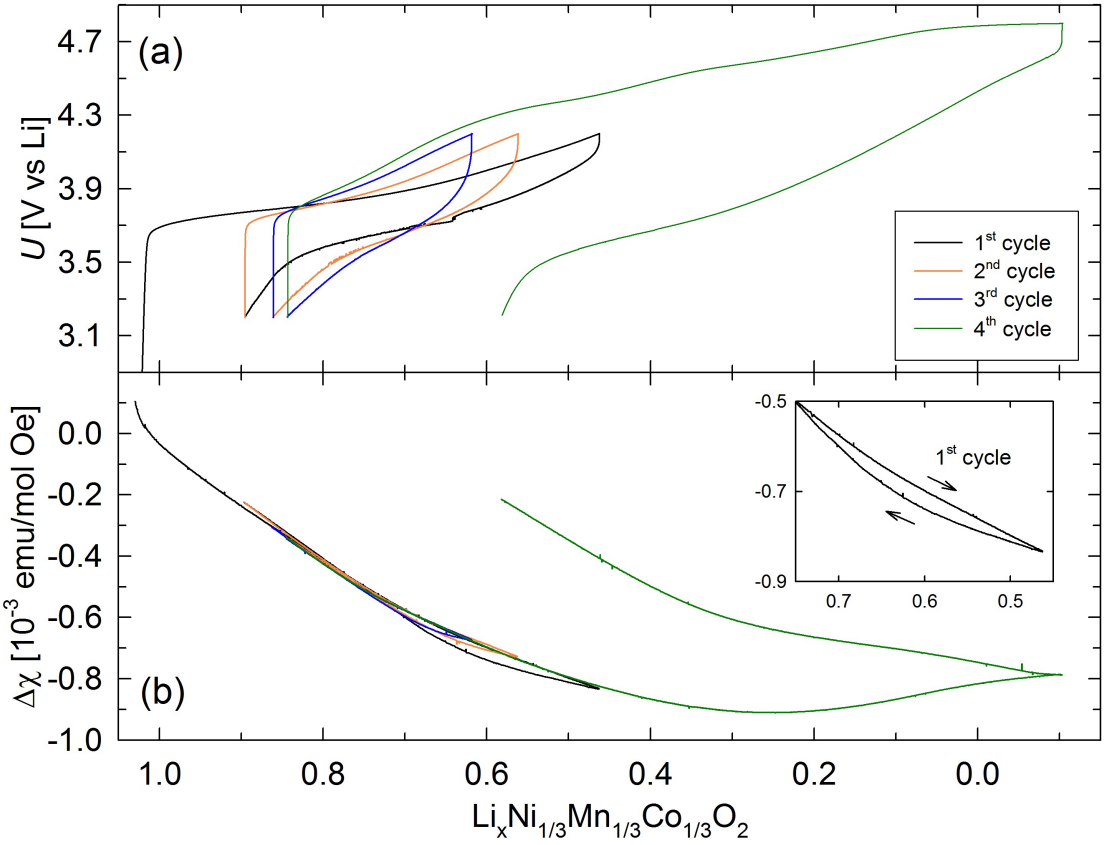

Figure 4.3: Replotted magnetic susceptibility measurements of Fig. 4.2
(a) Electrode potential U and (b) magnetic susceptibility $\Delta\chi$ as a function of Li concentration x in $Li_xNi_{1/3}Mn_{1/3}Co_{1/3}O_2$ during 4 consecutive cycles of charging and discharging with cut off potentials 3.2 and 4.2 V (cycles one to three) and the increased upper cut off potential of 4.8 V (4^{th} cycle). The apparent negative Li contents at the end of the charging arises due to the assumption that the current is entirely caused by Li extraction and thus excluding electrolyte oxidation process which will occur at potentials higher than 4.65 V [70, 71]. Note: for clarity in the insert only the first cycle is shown.

rate until $t = 47.8$ h. Further Li extraction results in a reduced decrease of χ with a flattening at 51.7 h and a subsequent χ-reincrease which emerges in a linear increase for $t = 53$ h until the upper cut off potential of 4.8 V is reached ($t = 58.6$ h). Upon the onset of discharging the linear χ-increase proceeds ($t = 58.6 - 64.7$ h) followed by a transition between $t = 64.7$ and 66.9 h to a higher constant rate for $t > 66.9$ h until the lower cut off potential of 3.2 V is reached at $t = 71.8$ h.

The data in Fig. 4.2 have been replotted as a function of the Li content x in Fig. 4.3, which was calculated for the nominal cathode mass with Faraday's law under the assumption that the current is entirely caused by Li extraction/insertion. For the first three charging cycles the χ-curves perfectly overlap. For high Li contents also the charging and discharging overlap, whereas for lower Li contents a hysteresis-

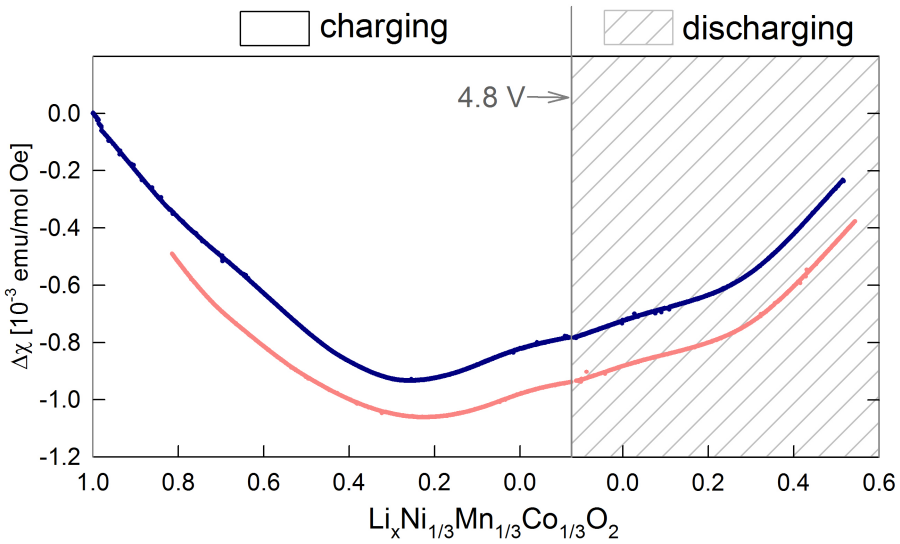

Figure 4.4: Comparison of two cells charged to 4.8 V
Change in magnetic susceptibility $\Delta\chi$ of another $Li_xNi_{1/3}Mn_{1/3}Co_{1/3}O_2$ cathode as a function of Li content x with cut off potentials 4.8 and 3.2 V for the first charging cycle (blue) in comparison to the 4^{th} charging cycle of the cathode according to in Fig. 4.2 (red). Note: For a better comparison the replotted data (red dots) have been shifted by $-1.5 \cdot 10^{-4}$ emu/mol Oe.

like behavior occurs between the reversing point on the right–hand side and about $x = 0.71$ (see insert in Fig. 4.3b). Also $\chi(x)$ for the 4^{th} charging cycle (with upper cut off potential 4.8 V) agrees with the previous observed charging cycles, but the subsequent discharging cycle is not congruent to the discharging cycles one to three. This discrepancy arises from the observed continuous increase at the beginning of the discharging cycle rather than a decrease what would be expected for a fully reversible process (see also Fig. 4.2).

To verify this discrepancy at low Li contents another cell was charged to 4.8 V (within the first cycle) and subsequently discharged down to 3.2 V. A comparison between this and the previously described measurement (see Fig. 4.3) can be found in Fig. 4.4. Both measurements show the same variation of χ proving the reproducibility and reliability of the observed results.

4.1.2 $Li_xNi_{0.6}Mn_{0.2}Co_{0.2}O_2$

Figure 4.5 shows the variation of the magnetic susceptibility $\Delta\chi$ together with the electrode potential U as a function of charging time t for five consecutive cycles of charging and discharging of $Li_xNi_{0.6}Mn_{0.2}Co_{0.2}O_2$ with different charging rates. Cycles

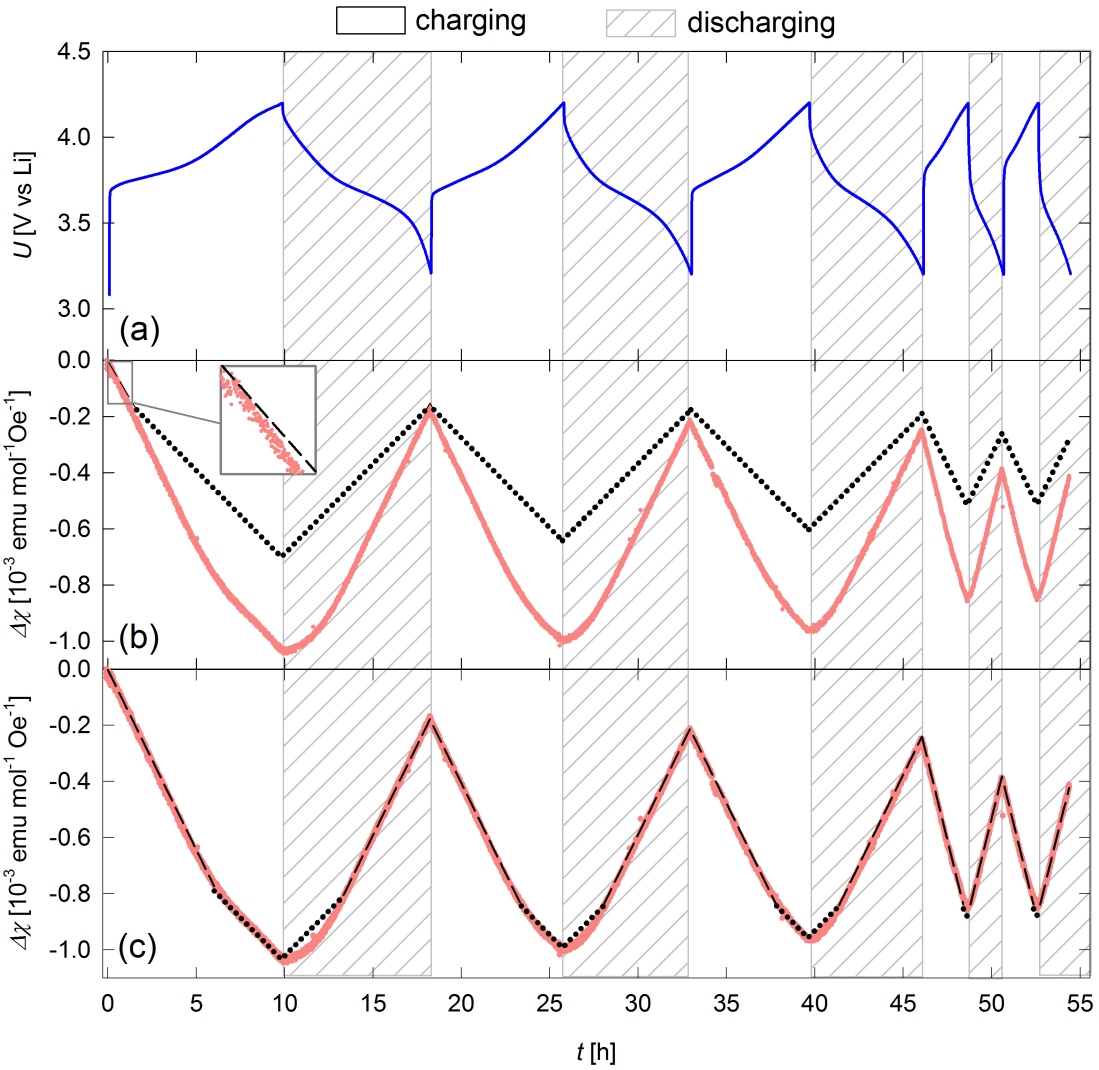

Figure 4.5: Magnetic susceptibility measurements of $Li_xNi_{0.6}Mn_{0.2}Co_{0.2}O_2$
Five consecutive cycles of charging and discharging of the cathode material $Li_xNi_{0.6}Mn_{0.2}Co_{0.2}O_2$. Cycles 1-3 were charged/discharged with a C/10-rate and cycles 4-5 with a C/5-rate. (a) Electrode potential U (cut off potentials 4.2 and 3.2 V) and (b) change in the magnetic susceptibility $\Delta\chi$. In (c) the same data as in (b) are displayed as gray circles. The straight lines of the simple model (b) and the proposed model (c) are calculated according to Eq. (2.18) and the concentrations of the transition metal ions in the respective oxidation state according to Tab.5.1b. (b) $Ni^{2+}(S = 1) \rightarrow Ni^{3+}(S = 1/2)$ oxidation (black dashed line) and $Ni^{3+}(S = 1/2) \rightarrow Ni^{4+}(S = 0)$ oxidation (black dotted line). (c) A simultaneous $Ni^{2+}(S = 1) \rightarrow Ni^{3+}(S = 1/2)$ and $Co^{2+}(S = 3/2) \rightarrow Co^{3+}(S = 0)$ oxidation (black dashed line) and $Ni^{3+}(S = 1/2) \rightarrow Ni^{4+}(S = 0)$ oxidation (black dotted line).

1-3 have been performed with a C/10-rate and cycles 4-5 with a C/5-rate. With the onset of charging χ immediately starts to decrease. For the first 6 hours this decrease prevails in a linear manner, followed by a linear decrease with reduced rate until the end of the first charging cycle (total charging time $t = 10$ h). Like for

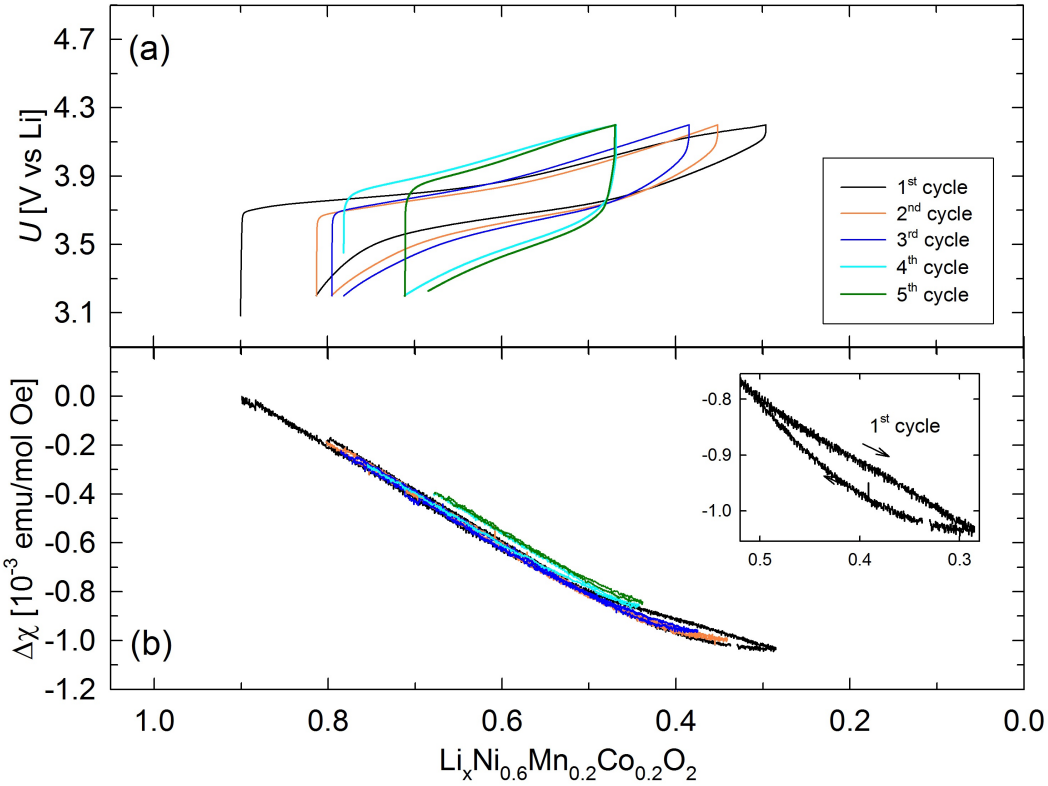

Figure 4.6: Replotted magnetic susceptibility measurements of Fig. 4.5
(a) Electrode potential U and (b) change in the magnetic susceptibility $\Delta\chi$ of the cathode material $Li_xNi_{0.6}Mn_{0.2}Co_{0.2}O_2$ as a function of the Li content x. Cycles 1-3 were charged/discharged with a C/10-rate and cycles 4-5 with a C/5-rate.

$Li_xNi_{1/3}Mn_{1/3}Co_{1/3}O_2$ reversing the current flow (discharging) instantaneously results in a χ increase. This increase at first is monotonously between 10 h and 14 h followed by a linear steeper increase until the end of the discharging cycle at $t = 18$ h. For the subsequent two charging/discharging cycles the χ-variation is qualitatively the same. At $t = 45.9$ h, the beginning of the 4^{th} charging cycle (C/5-rate), the χ decrease is analogous to charging cycles 1-3 described by two consecutive linear decreases, the former of which (45.9 h and 48.4 h) with a higher rate. In the following discharging cycles the observed χ-variation is in the reversed order: a linear increase first with reduced rate between 48.6 and 48.8 h followed by a higher rate until the end of the discharging cycle at $t = 50.6$ h. For the 5^{th} cycle the χ-variation is qualitatively the same as in the 4^{th} cycle. Note, the rate of linear χ-variation in cycles four and five is twice as high as the observed linear rate in the corresponding regions of cycles one to three.

In Fig. 4.6, $\Delta\chi$ and U are plotted as a function of the Li content x, which is calculated for the nominal cathode mass using Faraday's law under the assumption that the

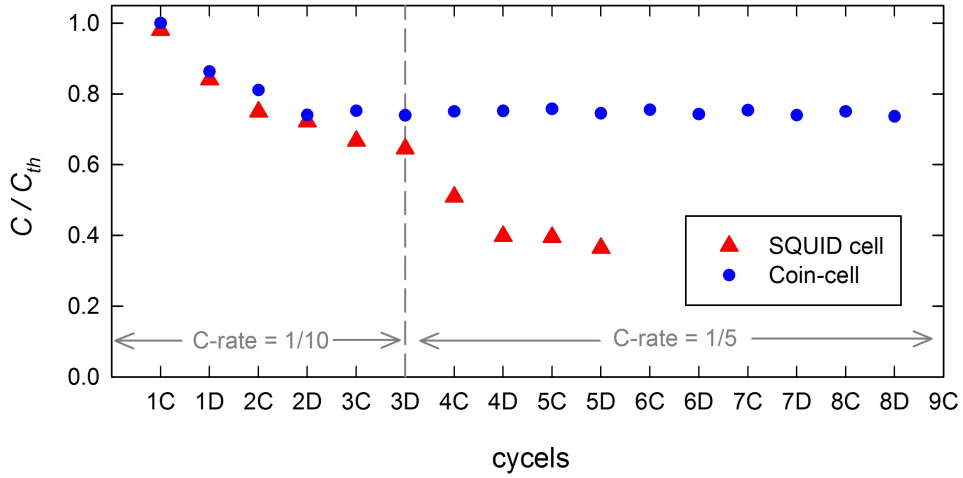

Figure 4.7: Comparison of a coin-cell and a SQUID-cell measurement
Nominal capacity of the charging (C) and the discharging (D) cycles of a coin–cell measurement (blue circles) and the SQUID measurement (red triangles, obtained from Fig. 4.5). The coin–cell measurement was performed by H. Kren from VARTA Micro Innovation GmbH using the same cathode material as was used for the SQUID measurement.

current is entirely caused by Li extraction/insertion. Although $U(x)$ agrees with the expected charging curve for $Li_xNi_{0.6}Mn_{0.2}Co_{0.2}O_2$ cathodes, the individual charging as well as the discharging curves do not overlap perfectly for the different cycles, especially for higher charging rates. While the observed capacity loss (U_{max}/U_{min} is reached for higher/lower Li contents compared to the previous charging cycle) during charging with a C/10-rate is expected as it is a common problem for $LiNi_{0.6}Mn_{0.2}Co_{0.2}O_2$ cathodes [4, 5], the high losses for the higher charging rate C/5 arise most likely from the rather thick electrodes used in the SQUID cell, necessary to increase the magnetic response (see Fig. 4.7 for a comparison between the capacity deduced from the SQUID cell measurement and that under ideal condition). On the other hand, the $\Delta\chi(x)$-curves of various cycles perfectly overlap (Fig. 4.6). For Li contents $x > 0.53$ also the discharging and charging within one cycle overlap, whereas for Li contents $0.5 > x \geq 0.3$ a hysteresis–like behavior (most pronounced in the first cycle, see insert in Fig. 2b) occurs between the charging and discharging cycle.

Similar to $Li_xNi_{1/3}Mn_{1/3}Co_{1/3}O_2$ the lower Li concentration region of the cathode material was studied, by increasing the upper cut off potential to 4.8 V. Figure 4.8 displays the electrode potential U together with the variation of the magnetic susceptibility $\Delta\chi$ for one cycle (out of two) charged between 3.2 and 4.8 V. Within the first 10.8 h of charging, the χ-variation is the same as for the measurement presented in Fig. 4.5. Upon further Li extraction ($t > 10.8$ h), $\Delta\chi$ first flattens and subsequently

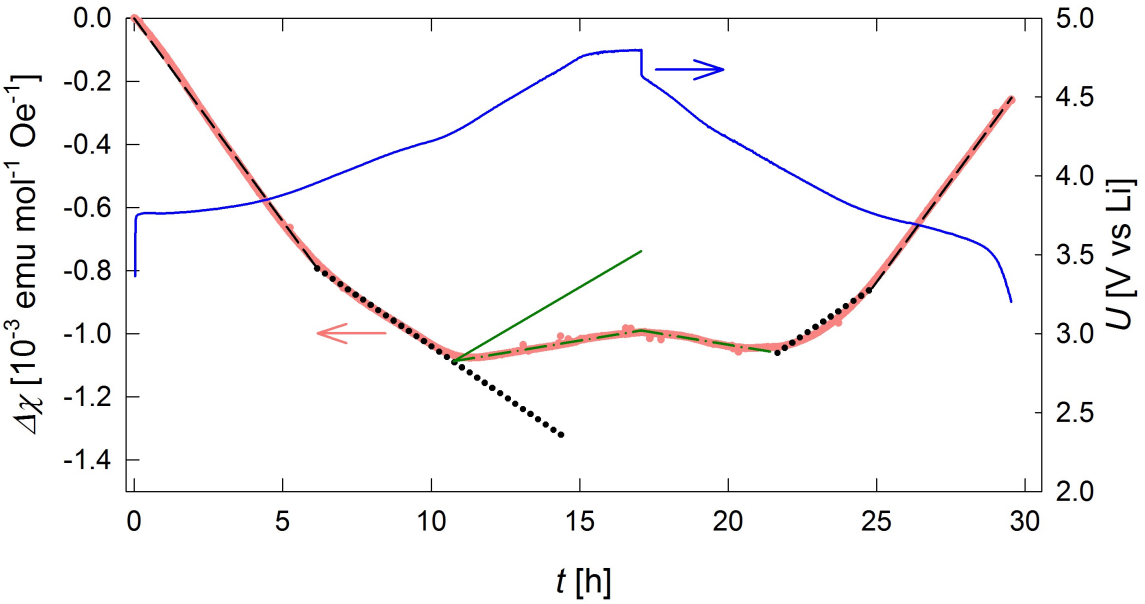

Figure 4.8: Effect of high cut-off potentials for $Li_xNi_{0.6}Mn_{0.2}Co_{0.2}O_2$
Electrode potential U (blue line) and change in the magnetic susceptibility $\Delta\chi$ (red circles) of the $Li_xNi_{0.6}Mn_{0.2}Co_{0.2}O_2$ cathode as a function of charging time t for the first charging/discharging cycle with cut off voltages 4.8 V and 3.2 V. The straight lines are calculated according to Eq. (2.18) for a simultaneous oxidation of $Ni^{2+}(S = 1) \rightarrow Ni^{3+}(S = 1/2)$ and $Co^{2+}(S = 3/2) \rightarrow Co^{3+}(S = 0)$ (black dashed line), and subsequent oxidation of $Ni^{3+}(s = 1/2) \rightarrow Ni^{4+}(S = 0)$ (black dotted line) and of $Co^{3+}(S = 0) \rightarrow Co^{4+}(S = 1/2)$ (green line). Green dash-dotted line denotes a contribution to the oxidation of $Co^{3+}(S = 0) \rightarrow Co^{4+}(S = 1/2)$ by O- or Ni-ions. Note: the Li extraction process lasts longer than predicted by Faraday's law. For potentials $U \geq 4.65$ V a fraction of charge is being lost due to electrolyte oxidation [70, 71]. Thus, the green line was corrected in such a way that the end of the charging cycle at 4.8 V corresponds to a complete Li extraction.

re-increases again until the end of the charging cycle ($t = 17.1$ h). During the following discharging cycle the χ-variation occurs in the reversed order.

4.1.3 Ex-situ measurements

For both cathode materials, $Li_xNi_{1/3}Mn_{1/3}Co_{1/3}O_2$ and $Li_xNi_{0.6}Mn_{0.2}Co_{0.2}O_2$, the magnetic susceptibilities for different Li contents were measured ex-situ in dependence of temperature. For $Li_xNi_{1/3}Mn_{1/3}Co_{1/3}O_2$, the inverse of the magnetic susceptibility $1/\chi$ for the Li contents $x = 1.03$, 0.45, and 0.33 is displayed in Figure 4.9a. In the case of $Li_xNi_{0.6}Mn_{0.2}Co_{0.2}O_2$, $\chi(T)$ was measured for $x = 0.90$, 0.81, 0.64, 0.46, 0.41, 0.29, and 0.16, the Li contents $x = 0.90$, 0.46, and 0.29 of which, are presented in Fig. 4.9b. For both cathode materials the ex-situ measurement have been background corrected

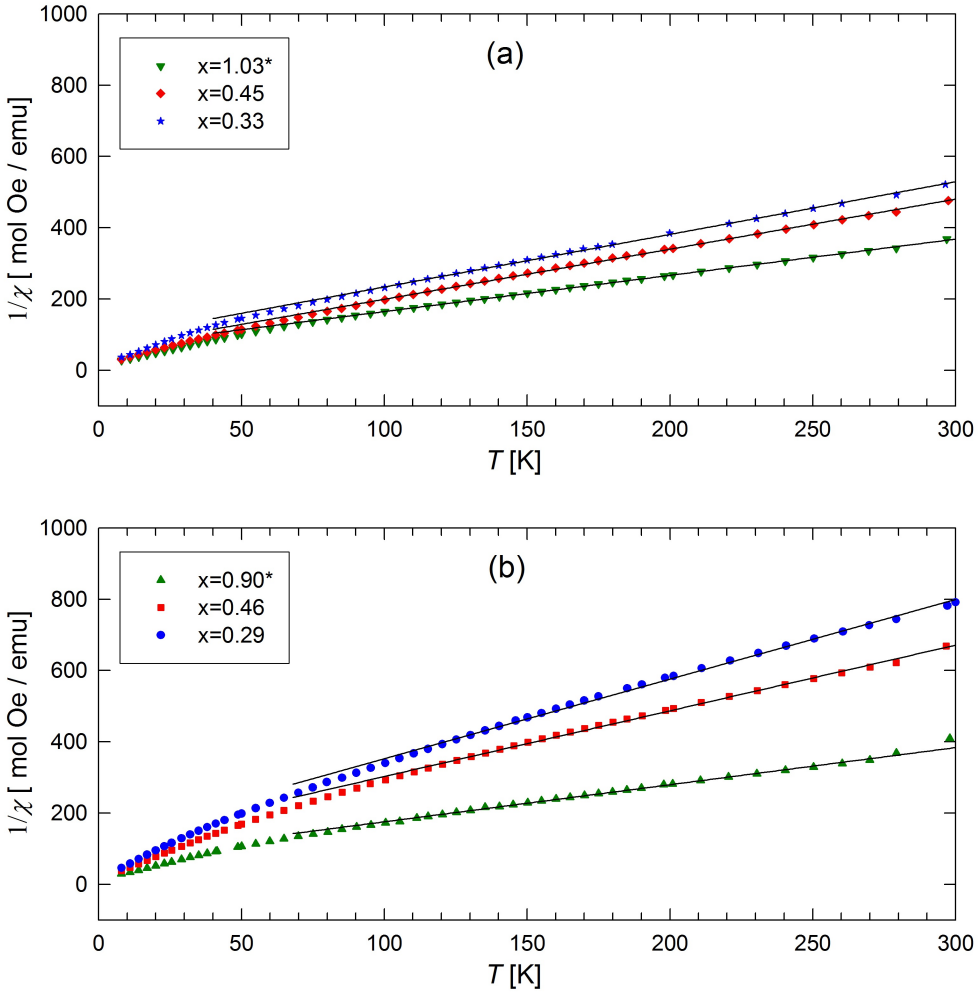

Figure 4.9: Temperature dependent magnetic susceptibility ex-situ measurements
Inverse of the magnetic susceptibility χ of (a) $Li_xNi_{1/3}Mn_{1/3}Co_{1/3}O_2$ and (b) $Li_xNi_{0.6}Mn_{0.2}Co_{0.2}O_2$ cathode as a function of temperature T for three different Li contents measured in field cooling mode at a constant magnetic field of 5 kOe. The black lines are least square fits to $1/\chi(T)$ in the temperature range between 75 K and 300 K in (a) and 100 K and 300 K in (b), using Eq. (2.15).
* Initial state as revealed by ICP-MS analysis.

for the magnetic moment of the aluminum substrate as well as for the binder and the carbon black analogous to the procedure described in Ref. [40]. The analysis of the results is given in the discussion (section 5.1.1).

4.1.4 $Na_xV_2(PO_4)_3$

Figure 4.10 shows the electrode potential U and the change in the magnetic susceptibility $\Delta\chi$ (with respect to the magnetic signal of the pristine sample) as a function of

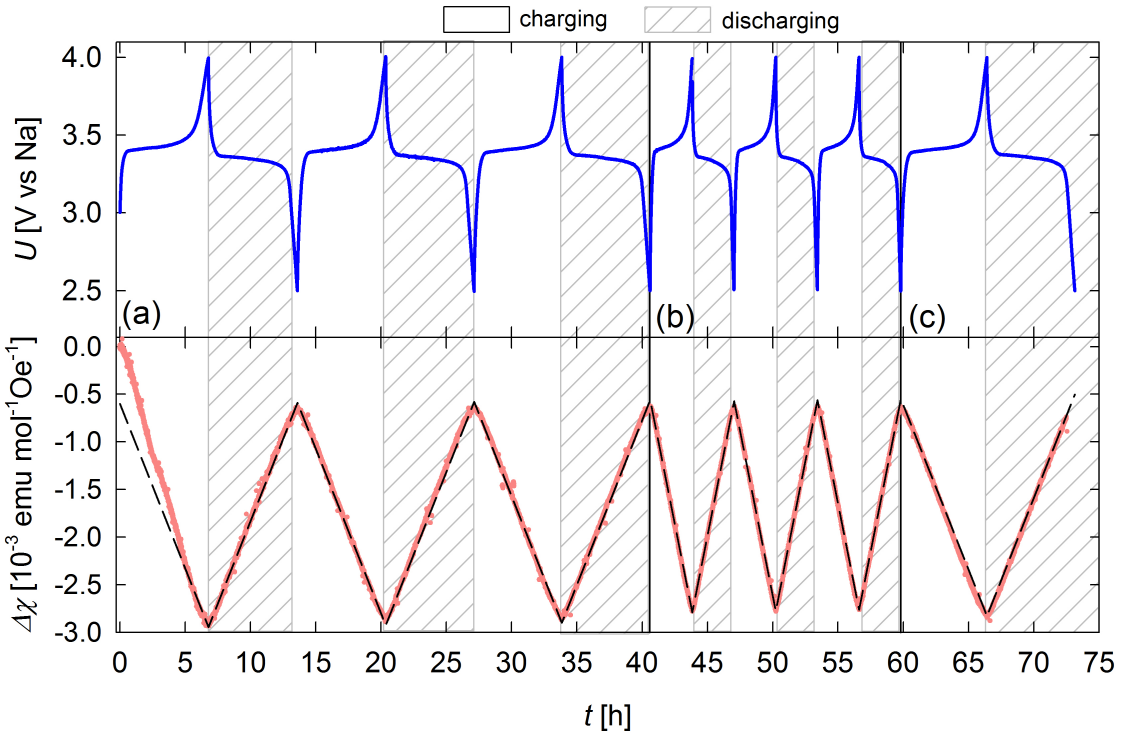

Figure 4.10: Magnetic susceptibility measurements of $Na_xV_2(PO_4)_3$
Electrode potential U with the cut off potentials 4.0 and 2.5 V and change in the magnetic susceptibility $\Delta\chi$ as a function of charging time t for seven consecutive cycles of charging and discharging of the cathode material $Na_xV_2(PO_4)_3$. The straight lines are calculated according to Eq. (2.18) assuming exclusive $V^{3+}(S = 1) \rightarrow V^{4+}(S = 1/2)$ oxidation. The charging rates (C-rates) where chosen to be of (a) C/6 (b) C/3 and (c) C/6.

charging time t for seven consecutive cycles with different charging rates. With the onset of charging χ immediately starts to decrease. This decrease prevails monotonously until the upper cut-off potential of 4.0 V is reached after 6.8 h of charging. Reversing the current flow results in an instantaneous linear re-increase of χ, which lasts until the end of the discharging cycle at t=13.6 h. The second and third cycle qualitatively show the same linear variation of the magnetic susceptibility. Doubling the charging/discharging current (cycles 4-6) results in a linear decrease/increase of χ during charging/discharging the slope of which being also doubled. In the subsequent seventh cycle the charging current was, again, chosen in the same way as in cycles 1-3. This reproduces the χ-variation observed in cycles 2-3.

In Fig. 4.11a and b the first three cycles of a freshly prepared further cell are shown. The observed χ-variation is exactly the same as outlined before. Apart from the first cycle the variation of χ is linear (decrease for charging and increase for discharging). Figures 4.11c and 4.11d show cycles number 25 to 28 of yet another cell. It should

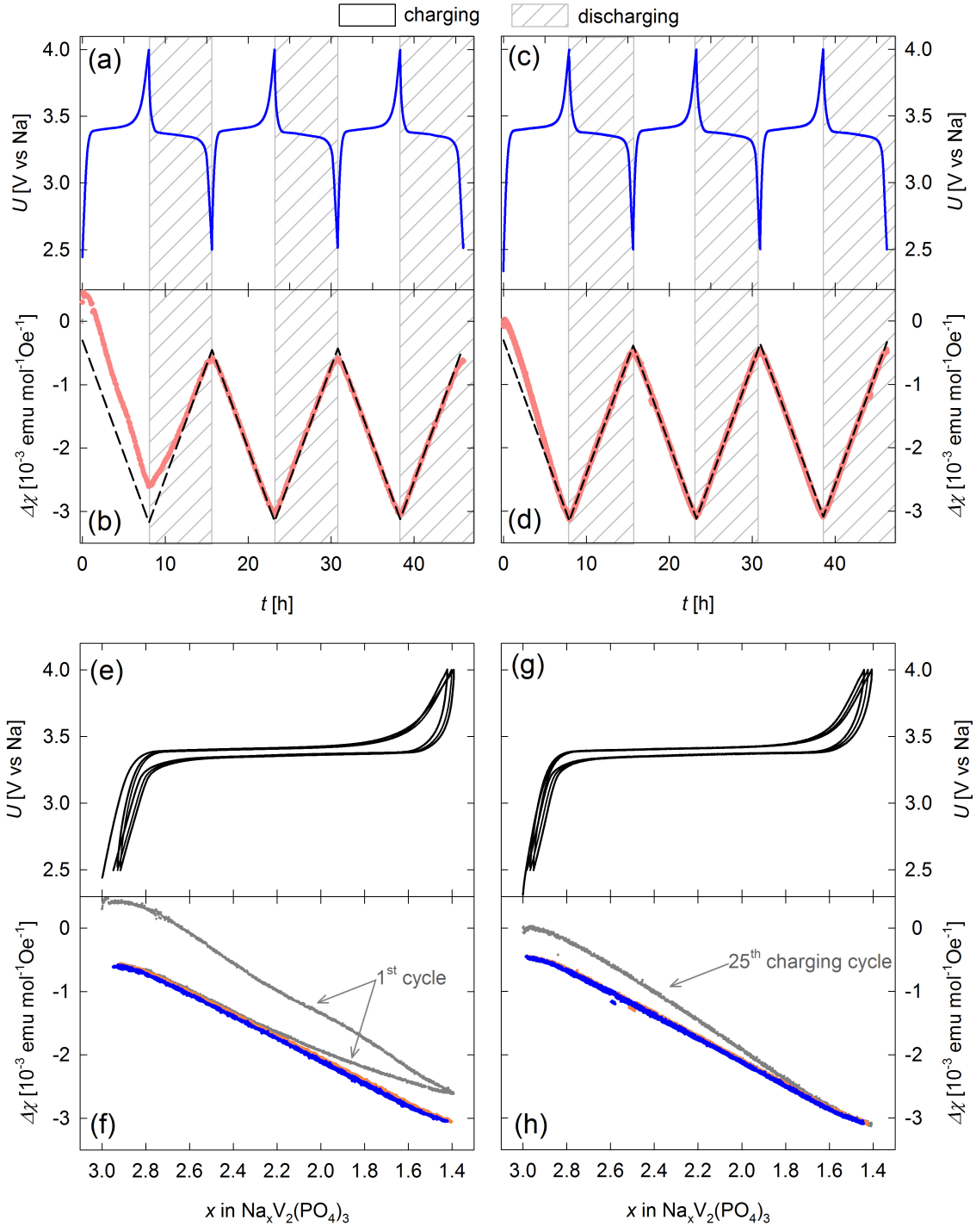

Figure 4.11: Charging/discharging measurements on $Na_xV_2(PO_4)_3$
Same conditions as in Fig. 4.10, but all three measurements (4.10, 4.11a,b and 4.11c,d) performed with different cells. (a),(b)/(c),(d): charging cycles 1-3/24-27, respectively. The straight dashed line in (b) and in (d) are calculated according to Eq. (2.18) assuming exclusive $V^{3+}(S = 1) \rightarrow V^{4+}(S = 1/2)$ oxidation. In (e)-(f) the change in the magnetic susceptibility $\Delta\chi$ and electrode potential U is replotted as a function of the Na content x.

be noted that there was a time difference between cycle number 24 and 25 of 6 days. The observed susceptibility variation in Fig. 4.11c can be described as above (Fig. 4.11b).

The data represented in Figs. 4.11(a)-(d) are replotted in Figs. 4.11(e)-(h) as a function of the sodium content x, which is calculated for the nominal cathode mass using Faraday's law and the assumption that the entire current is consumed for Na extraction and insertion, respectively. While the electrode potential curve of different charging and discharging cycles overlaps (see Fig. 4.11), the change in the magnetic susceptibility (displayed in Figs. 4.11f and h) differs between the first and second cycle. However, from the second cycle onwards $\Delta\chi$ perfectly overlaps for various charging and discharging cycles.

4.2 Charging induced defects in $Li_xNi_{1/3}Mn_{1/3}Co_{1/3}O_2$

Figure 4.12 displays the electrode potential U and the change in positron lifetime $\Delta\tau$ as a function of the Li content x and the charging time t, respectively, for three measurements with different charging profiles of $Li_xNi_{1/3}Mn_{1/3}Co_{1/3}O_2$. The measurements presented in Fig. 4.12a have been obtained by continuously charging the battery, while in Fig. 4.12b after a pre-defined charging time of 5 hours charging was interrupted for another 5 hours during which the positron lifetime measurement was performed (under open circuit conditions). Both measurements reveal the same variation of the positron lifetime, hence, any influence of the charging current on the positron lifetime measurement can be excluded. $\Delta\tau(x)$ can be divided into four different substages. In stage I ($x > 0.87$) τ continuously increases. Following this increase, in stage II ($0.87 > x > 0.77$) no further increase but even a slight decrease of the positron lifetime can be discerned. Further lithium extraction, $0.77 > x > 0.63$, results again in a continuous increase if of the positron lifetime (stage III). Finally in stage IV ($x < 0.63$) the positron lifetime decreases.

In a next step the variation of the positron lifetime also for the discharging cycle was probed. Figure 4.12d displays the electrode potential U, the charging current i as well as the change in positron lifetime of $\Delta\tau$ of $Li_xNi_{1/3}Mn_{1/3}Co_{1/3}O_2$. For this measurement the same charging profile as for the measurement displayed in Fig. 4.12b was chosen: 5 hours charging and discharging, respectively, and 5 hours under open

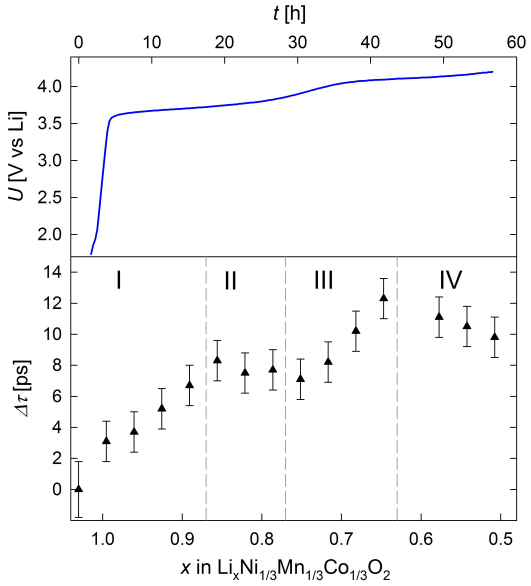

(a) **Sample A**

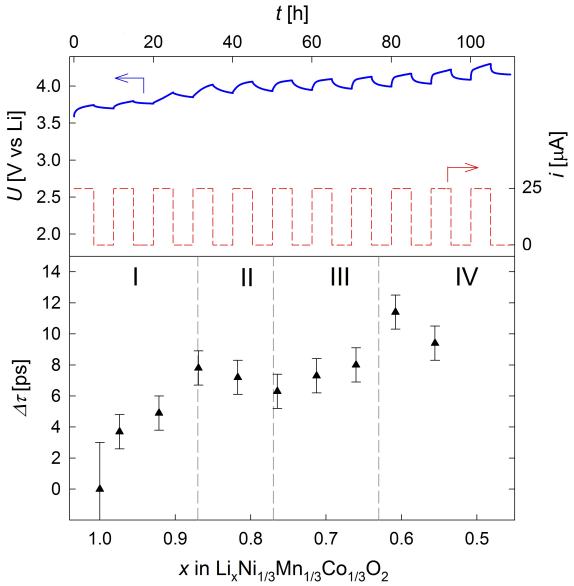

(b) **Sample B**

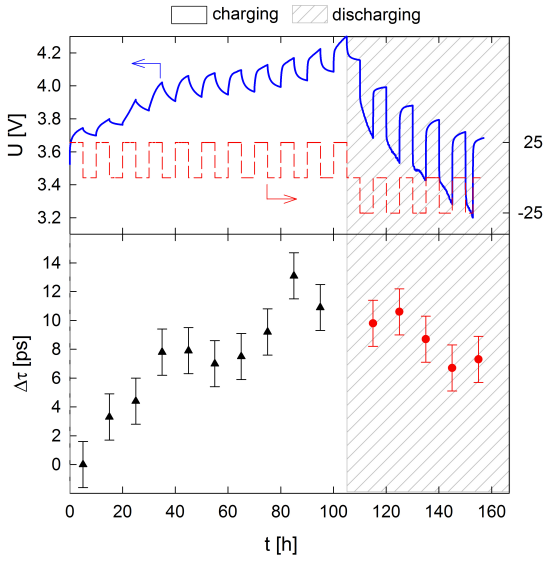

(c) **Sample C**

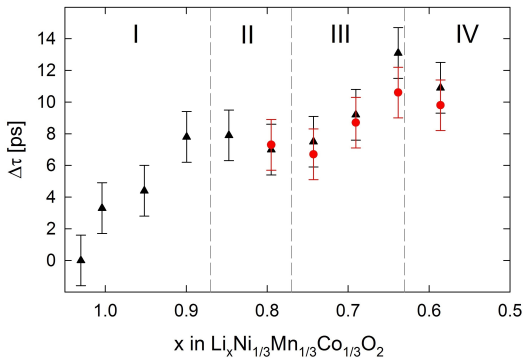

(c1) **Sample C**

Figure 4.12: Operando positron lifetime studies of $Li_xNi_{1/3}Mn_{1/3}Co_{1/3}O_2$
Electrode potential U and change in positron lifetime $\Delta\tau$ of three independent measurements of $Li_xNi_{1/3}Mn_{1/3}Co_{1/3}O_2$ as a function of charging time t and Li content x (C/50-rate). Sample A: Charging was performed continuously. Sample B: Charging was performed in a step-like manner (see charging current i): After a pre-defined charging step of 5 hours charging was stopped and the positron lifetime was measured under open circuit conditions for 5 hours before the next charging step was applied. Sample C: Analogous to sample B charging and discharging was performed in a step-like manner. (c1) The change in positron lifetime as a function of Li content x of Sample C (charging: black triangles, discharging: red circles).

circuit conditions during which the positron lifetime measurement was performed. The observed overall charging curves agrees with the expected charging curves for $Li_xNi_{1/3}Mn_{1/3}Co_{1/3}O_2$ cathodes. However, as can be seen in Fig. 4.12d after each charging step (during open circuit conditions) U relaxes towards lower potential values indicating a slight over-potential necessary for battery charging. This over-potential increases up to 400 mV during discharging, which results in an incomplete discharging cycle. The variation of τ within the charging cycle again revealed the 4 substages described above and are fully reversible in the discharging cycle.

CHAPTER 5

Discussion

In following the measurements presented in chapter 4 will be discussed. First, in section 5.1 the discussion of the charge compensation process in $Li_xNi_{1/3}Mn_{1/3}Co_{1/3}O_2$ and $Li_xNi_{0.6}Mn_{0.2}Co_{0.2}O_2$ is presented, followed by that of the post-Li-ion cathode material $Na_xV_2(PO_4)_3$ (5.2). At the end, the operando positron annihilation experiments on $Li_xNi_{1/3}Mn_{1/3}Co_{1/3}O_2$ are discussed in section 5.3.

As already stated at the beginning of chapter 4, parts of the discussions are already published and are reprinted from [G. Klinser, S. Toplovec, H. Kren, S. Koller, W. Goessler, H. Krenn and R. Würschum, Appl. Phys. Lett. **109** (2016) 213901], with the permission of AIP Publishing and from [G. Klinser, M. Stückler, H. Kren, S. Koller, W. Goessler, H. Krenn and R. Würschum, J. Power Sources **396** (2018) 791] or have recently been accepted in Appl. Phys. Lett. **114** (2019) 000000.

5.1 Charge compensation process in $Li_xNi_{1/3}Mn_{1/3}Co_{1/3}O_2$ and $Li_xNi_{0.6}Mn_{0.2}Co_{0.2}$

State of the art

As outlined in the introduction one of the open questions in these cathode materials is the charge compensation process. Although various ex-situ and in-situ measurement techniques, such as X-ray photoelectron spectroscopy [22], X-ray absorption spectroscopy [23–33], nuclear magnetic resonance spectroscopy [33], electron paramagnetic resonance spectroscopy [34–36], electron energy loss spectroscopy [37], magnetom-

etry [31, 34, 36, 39] or theoretical calculations [30, 38] have been applied, so far, no consistent notion exists.

For $Li_xNi_{1/3}Mn_{1/3}Co_{1/3}O_2$ the initial state (x=1) was concluded to be Ni^{2+}(S=1), Mn^{4+}(S=3/2) and Co^{3+}(S=0) respectively [24–26, 32–34, 38, 39, 62]. Based on this initial state in the high Li concentration region ($x > 1/3$) it was concluded, on the one hand, that only Ni- ions contribution to the charge compensation process. However, it is not clear if Ni-ions are oxidized in a step-like sequence of $Ni^{2+} \rightarrow Ni^{3+}$ for $1 \geq x \geq 2/3$ and $Ni^{3+} \rightarrow Ni^{4+}$ for $2/3 > x > 1/3$ [25, 30, 34, 38] or by a two-electron conversion $Ni^{2+} \rightarrow Ni^{4+}$ for $1 \geq x \geq 1/3$ [22, 27, 29, 39]. On the other hand, a simultaneous oxidation of Ni- and Co-ions [24, 26, 28, 31, 35, 36] or of Ni- and O-ions [32, 33] is reported. The charge compensation process for low Li contents $x < 1/3$ is even more controversial: Discussed are a oxidation of either Co-ions [26, 30, 34, 38] or O-ions [23, 25, 32, 37], exclusively, or else of Co- and O-ions simultaneously [33].

The charge compensation process for the Ni-rich cathode $Li_xNi_{0.6}Mn_{0.2}Co_{0.2}O_2$ is not yet understood either. Primarily the red-ox couples Ni^{2+}/Ni^{3+}, Ni^{3+}/Ni^{4+} and Co^{3+}/Co^{4+} are supposed to be involved, as it is the case for $Li_xNi_{1/3}Mn_{1/3}Co_{1/3}O_2$ [25, 30, 34, 72] or $Li_xNi_{0.65}Co_{0.25}Mn_{0.1}O_2$ [73]. The unclear charge compensation process is mainly owed the lack of a consistent theory for the initial state. It was concluded that the initial state consists of $Li^+Ni^{2+}_{0.2}Ni^{3+}_{0.4}Mn^{4+}_{0.2}Co^{3+}_{0.2}O^{2-}_2$ [42], but also the presence of Co^{2+} and an increased amount of Ni^{2+} was reported [43].

In order to clarify the charge compensation process, operando magnetic susceptibility measurements in a SQUID magnetometer were applied as presented in section 4.1. To emphasize once more, magnetic measurements not only have the advantage of probing the bulk of the material rather than surface near areas, but are also specific and sensitive to the oxidation state of the transition metal ions.

5.1.1 Low-potential region (cut-off potentials 3.2 V and 4.2 V)

For both cathode materials, $Li_xNi_{1/3}Mn_{1/3}Co_{1/3}O_2$ and $Li_xNi_{0.6}Mn_{0.2}Co_{0.2}O_2$, prevalence of pure Langevin paramagnetism at room temperature according to Eq. (2.15) was confirmed by temperature-dependent magnetic susceptibility measurements (see Fig. 4.9). Fitting the $\chi(T)$-data of the pristine sample using Eq.(2.15) yields for $Li_xNi_{1/3}Mn_{1/3}Co_{1/3}O_2$ a mean effective magnetic moment of $\overline{\mu}_{eff} = 2.80\,\mu_B$ and a

Curie-Weiss temperature of $\Theta = 54\,\mathrm{K}$. Analogous for $\mathrm{Li}_x\mathrm{Ni}_{0.58}\mathrm{Mn}_{0.22}\mathrm{Co}_{0.2}\mathrm{O}_2$ values of $\overline{\mu}_{eff} = 2.71\,\mu_B$ and $\Theta = 60\,\mathrm{K}$ were observed. For both cathode materials the observed Curie-Weiss temperatures are considered as constant because, in each case, no notable change of Θ was observed between the samples with different Li contents.[1]

$\mathbf{Li}_x\mathbf{Ni}_{1/3}\mathbf{Mn}_{1/3}\mathbf{Co}_{1/3}\mathbf{O}_2$

The experimental value of $\overline{\mu}_{eff} = 2.80\,\mu_B$ obtained from ex-situ measurements is close to the theoretical value of $2.77\,\mu_B$ (calculated from Eq. (2.18) and the concentrations presented in Table 5.1a). Thus, the transition metal oxidation states of the pristine sample are confirmed to be Ni^{2+}(S=1), Mn^{4+}(S=3/2) and Co^{3+}(S=0) respectively, as reported in literature [24–26, 32–34, 38, 39, 62]. Moreover, as can be seen in Table 5.1a also for the samples with lower Li concentrations the experimental obtained values μ_{exp} are in good agreement with the theoretical values μ_{eff}, which are calculated for a subsequent oxidation processes of $Ni^{2+}(S = 1) \rightarrow Ni^{3+}(S = 1/2)$ for $1 \geq x > 2/3$ followed by $Ni^{3+}(S = 1/2) \rightarrow Ni^{4+}(S = 0)$ for $2/3 > x > 1/3$. This indicates a consecutive oxidation process of Ni^{2+} followed by Ni^{3+}. However, from the present ex-situ measurements a two-electron conversion ($Ni^{2+} \rightarrow Ni^{4+}$) or a contribution of Co- or O-ions to the charge compensation process cannot be excluded.

This point is clarified by applying the consecutive oxidation process model to the operando measurements. Using Eq. (2.18), the first linear part (dashed line) in Fig. 4.2 is, thus, obtained under the aforementioned assumption that exclusively the oxidation reaction $Ni^{2+}(S = 1) \rightarrow Ni^{3+}(S = 1/2)$ occurs for $1 \geq x \geq 2/3$. After complete oxidation of Ni^{2+} to Ni^{3+}, which is obtained for $x = 2/3$ (gray dash-dotted horizontal line in Fig. 4.2), $Ni^{3+}(S = 1/2) \rightarrow Ni^{4+}(S = 0)$ oxidation is expected upon further charging resulting in a reduced slope (black dotted line) according to Eq. (2.18) and Table 5.1a. This predicted $\chi(t)$-variation perfectly fits the experimental data for Li contents $x > 0.71$ ($t < 5.5\,\mathrm{h}$) and $x < 0.64$ ($t > 6.9\,\mathrm{h}$), apart form the initial strong $\chi(t)$-decrease. Therefore, for the charge compensation process upon charging up to 4.2 V the following three step process can be concluded: (i) first, an exclusive oxidation of $Ni^{2+} \rightarrow Ni^{3+}$ for $x > 0.71$, (ii) followed by a simultaneous oxidation of Ni^{2+} and Ni^{3+} between $0.71 \geq x \geq 0.64$ until Ni^{2+} is completely oxidized, and (iii) finally a sole oxidation of $Ni^{3+} \rightarrow Ni^{4+}$ till the end of the charging cycle. A notable contribution of Co- or O-ions in the charge compensation process in this regime can be excluded, as this would manifest in a reduced decrease of $\chi(t)$.

[1] Note: The Curie-Weiss temperatures $\Theta = 54\,\mathrm{K}$ ($\mathrm{Li}_x\mathrm{Ni}_{1/3}\mathrm{Mn}_{1/3}\mathrm{Co}_{1/3}\mathrm{O}_2$) and $\Theta = 60\,\mathrm{K}$ ($\mathrm{Li}_x\mathrm{Ni}_{0.58}\mathrm{Mn}_{0.22}\mathrm{Co}_{0.2}\mathrm{O}_2$) are mean values of all ex-situ measurements.

Table 5.1: Effective magnetic moments μ_i of transition metal ions for the various oxidation states ($\mu_i = g\sqrt{S_i(S_i+1)}\mu_B$ with $g = 2$) of (a) $Li_xNi_{1/3}Mn_{1/3}Co_{1/3}O_2$ and (b) $Li_xNi_{0.58}Mn_{0.22}Co_{0.2}O_2$. For quoted concentrations c of transition metal ions the mean effective magnetic moment $\overline{\mu}_{eff}$ according to Eq. (2.18) as well as the obtained value $\overline{\mu}_{exp}$ from ex-situ measurements is given exemplary. For $Li_xNi_{0.58}Mn_{0.22}Co_{0.2}O_2$ the effective magnetic moment is given analogous to the model for $Li_xNi_{1/3}Mn_{1/3}Co_{1/3}O_2$ ($\overline{\mu}_{simple}$) and in addition with a model ($\overline{\mu}_{proposed}$) proposed by the author. Note: $c_{x=0.9}$ corresponds to the initial state as obtained from ICP-MS analysis.

(a) $Li_xNi_{1/3}Mn_{1/3}Co_{1/3}O_2$

		μ_i $[\mu_B]$	$c_{x=1}$	$c_{x=0.45}$	$c_{x=0.33}$
Ni^{2+}	(S=1)	2.83	1/3	0	0
Ni^{3+}	(S=1/2)	1.73	0	1/9	0
Ni^{4+}	(S=0)	0	0	2/9	1/3
Mn^{4+}	(S=3/2)	3.87	1/3	1/3	1/3
Co^{3+}	(S=0)	0	1/3	1/3	1/3
Co^{4+}	(S=1/2)	1.73	0	0	0
$\overline{\mu}_{exp}$ $[\mu_B]$			2.80	2.38	2.33
$\overline{\mu}_{eff}$ $[\mu_B]$			2.77	2.30	2.23

(b) $Li_xNi_{0.58}Mn_{0.22}Co_{0.2}O_2$

		μ_i $[\mu_B]$	$c_{x=0.9}$		$c_{x=0.46}$		$c_{x=0.29}$	
			simple	proposed	simple	proposed	simple	proposed
Ni^{2+}	(S=1)	2.83	0.12	0.33	0	0	0	0
Ni^{3+}	(S=1/2)	1.73	0.46	0.25	0.27	0.51	0.09	0.34
Ni^{4+}	(S=0)	0	0	0	0.31	0.07	0.49	0.24
Mn^{4+}	(S=3/2)	3.87	0.22	0.22	0.22	0.22	0.22	0.22
Co^{2+}	(S=3/2)	3.87	0	0.04	0	0	0	0
Co^{3+}	(S=0)	0	0.2	0.16	0.2	0.2	0.2	0.2
Co^{4+}	(S=1/2)	1.73	0	0	0	0	0	0
$\overline{\mu}_{simple}$ $[\mu_B]$			2.37		2.03		1.89	
$\overline{\mu}_{proposed}$ $[\mu_B]$				2.72		2.20		2.08
$\overline{\mu}_{exp}$ $[\mu_B]$			2.71		2.08		1.91	

Due to the kink-like variation of $\chi(t)$, also a direct oxidation $Ni^{2+}(S = 1) \rightarrow Ni^{4+}(S = 0)$ can be precluded because that would be associated with a single constant slope for $1 \geq x \geq 1/3$ in between that of $Ni^{2+} \rightarrow Ni^{3+}$ and $Ni^{3+} \rightarrow Ni^{4+}$. In the subsequent discharging cycle, the total variation of χ is also correctly described by Eq. (2.18) (straight lines in Fig. 4.2), which shows that the oxidation of Ni is completely reversible. The reduction occurs in the reversed order. The fact that the slope at the beginning of discharging is less pronounced (which manifests as hysteresis like behavior in Fig.

4.3b) than it would be expected for the reduction $Ni^{4+} \rightarrow Ni^{3+}$ may indicate kinetic effects which are supposed to be more relevant in the discharging cycle [70].

The initial strong χ-decrease in the first charging cycle right after the onset of Li extraction (left–most part in Fig. 4.2) indicates a slight overstoichiometry of the pristine electrode ($Li_{1+y}[Ni_{1/3}Mn_{1/3}Co_{1/3}]_{1-y}O_2$, $y = 0.03$) as evidenced by ICP-MS analysis. Indeed, a linear fit of the $\chi(t)$-data using Eq. (2.18) revealed a change of $\Delta\overline{\mu}^2_{eff} = 32\mu_B^2$ per extracted Li-ion. This value $\Delta\overline{\mu}^2_{eff}$ is consistent with a small amount of Co^{4+} (high spin) compensating the excess Li-ions because the reduction $Co^{4+}(S = 5/2) \rightarrow Co^{3+}(S = 0)$ upon Li extraction corresponds to $\Delta\overline{\mu}^2_{eff} = 35\mu_B^2$.

$Li_xNi_{0.6}Mn_{0.2}Co_{0.2}O_2$

In a first approach for $Li_xNi_{0.6}Mn_{0.2}Co_{0.2}O_2$ the same charge compensation process model (in the following referenced as simple model) as for $Li_xNi_{1/3}Mn_{1/3}Co_{1/3}O_2$ is applied: A consecutive oxidation processes of $Ni^{2+} \rightarrow Ni^{3+}$ until all Ni^{2+}-ions have been oxidized followed by the oxidation of $Ni^{3+} \rightarrow Ni^{4+}$ [25, 30, 34, 72]. Comparing the obtained values for the mean effective magnetic moment $\overline{\mu}_{exp}$ form fitting the $\chi(T)$-data presented in Fig. 4.9b using Eq. (2.15) with the calculated values for the simple model yields good agreements for lower Li^+ contents (see Table 5.1b). However, the value for the initial state $\overline{\mu}_{exp} = 2.71\mu_B$ significantly deviates from $\overline{\mu}_{simple} = 2.37\mu_B$ of that of the simple model. This discrepancy is even more obvious by comparing the χ-variation of the operando susceptibility measurement with that of the simple model. According to this model charging with a C/10-rate results in $Ni^{2+} \rightarrow Ni^{3+}$ oxidation within the first 1.9 hours (displayed as black dashed line in Fig. 4.5b) followed by $Ni^{3+} \rightarrow Ni^{4+}$ oxidation until the upper cut off potential of 4.2V is reached after 10 hours (black dotted line in Fig. 4.5b). Moreover, comparing the μ^2_{eff}-variation of the operando magnetic measurement of $Li_xNi_{0.6}Mn_{0.2}Co_{0.2}O_2$ with that of $Li_xNi_{1/3}Mn_{1/3}Co_{1/3}O_2$ (see Fig. 5.1) reveals two different rates. As obvious from Fig. 4.5b and Fig. 5.1, the experimental data cannot be correctly described with this simple model. On the one hand, the observed initial linear decrease of χ is more pronounced than that of an exclusive $Ni^{2+} \rightarrow Ni^{3+}$ oxidation (see Fig. 5.1 and insert in Fig. 4.5b). On the other hand, the predicted transition between $Ni^{2+} \rightarrow Ni^{3+}$ oxidation and $Ni^{3+} \rightarrow Ni^{4+}$ oxidation after 1.9 hours of charging (in Fig. 4.5b visible as a kink in the $\Delta\chi(t)$curve) is experimentally observed only after 6 hours of charging. Thus, it is obvious that the Ni^{2+}-ion concentration is underestimated for the initial state by this model. Enhanced

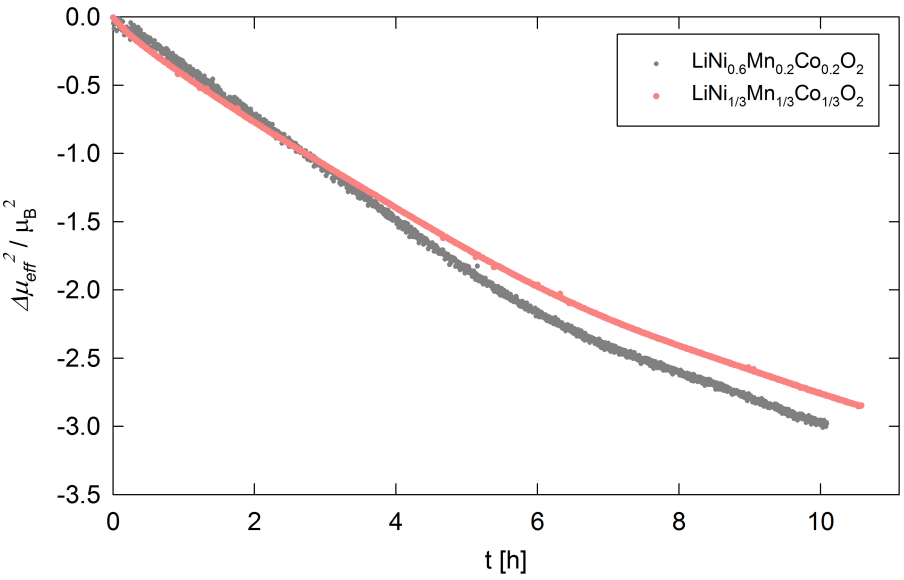

Figure 5.1: Comparison of $Li_xNi_{1/3}Mn_{1/3}Co_{1/3}O_2$ and $Li_xNi_{0.6}Mn_{0.2}Co_{0.2}O_2$
Comparison between the changes of the squared effective magnetic moment $\Delta\mu_{eff}^2$ of $Li_xNi_{0.6}Mn_{0.2}Co_{0.2}O_2$ and that of $Li_xNi_{1/3}Mn_{1/3}Co_{1/3}O_2$ as a function of charging time t. Note: In order to compare the two measurements the data for $Li_xNi_{1/3}Mn_{1/3}Co_{1/3}O_2$ have been multiplied by a factor of 1.16 which arises due to the different molar masses, Curie-Weiss temperatures and charging currents.

amounts of Ni^{2+}-ions for the initial state of $LiNi_{0.6}Mn_{0.2}Co_{0.2}O_2$ were predicted by computational methods ($Ni^{2+}/Ni^{3+} \approx 0.6$) [43] and by XAS- and RSXE measurements for the similar cathode material $LiNi_{0.65}Co_{0.25}Mn_{0.1}O_2$ ($Ni^{2+}/Ni^{3+} \approx 0.8$) [74].

A higher amount of Ni^{2+}-ions in the initial state may explain that the χ-kink is shifted to larger times compared to the simple model (i.e., 6 h instead of 1.9 h see Fig. 4.5b), however, it cannot account for the deviations in the rate of the χ-change for the first 6 hours of charging as seen in Fig. 5.1. In fact, the $\chi(t)$-variation associated with exclusive $Ni^{2+}(S = 1) \rightarrow Ni^{3+}(S = 1/2)$ oxidation is too low; $Ni^{3+}(S = 1/2) \rightarrow Ni^{4+}(S = 0)$ oxidation or a two electron conversion $Ni^{2+} \rightarrow Ni^{4+}$ would yield an even lower $\chi(t)$-variation. This leads to the conclusion that another ion has to be involved in the charge compensation process.

A more pronounced $\chi(t)$-decrease might arise from the oxidation of (i) Mn^{4+}-, (ii) Mn^{3+}-, or (iii) Co^{2+}-ions:

(i) Although $Mn^{4+}(S = 3/2) \rightarrow Mn^{5+}(S = 1)$ oxidation in principle would cause a stronger $\chi(t)$-decrease, Mn^{4+}-ions are considered to be electrochemical inactive in the charge compensation process of these compounds [44, 61, 75].

(ii) The experimental data could be fitted by assuming that 25% to the charge compensation process is due to oxidation of $Mn^{3+}(S = 2)$. Although, $Mn^{3+}(S = 2)$ was reported for the initial state of $LiNi_yCo_zMn_{1-y-z}O_2$ with different compositions ($x/y = 0.5/0.2$, $0.7/0.1$, $0.7/0.2$) [76], and $LiNi_{0.5}Mn_{0.15}O_{4-\delta}$ [77], a consecutive oxidation of first Mn^{3+} and then Ni^{3+} was reported for $LiNi_{0.5}Mn_{0.15}O_{4-\delta}$ [77], rather than a simultaneous oxidation, as invoked by the linear the $\chi(t)$-variation.

(iii) An obvious explanation of the pronounced decrease of χ appears to be given by the oxidation of high spin $Co^{2+}(S = 2)$ to low spin $Co^{3+}(S = 0)$. Co^{2+} was reported to be present in the initial state of Ni-rich cathodes, although in a low spin state ($S = 1/2$ rather 2) [73]. In fact, however, for octahedral coordinated Co^{2+}-ions, the high- and low-spin configurations are close in energy, whereas for Co^{3+} exclusively the $S = 0$ state is favorable [47, 78]. Therefore, a contribution of Co^{2+} to the charge compensation process seems most reasonable and will be considered further in the following, although from the present magnetic measurements the contribution from Mn-ions cannot be excluded. A further assessment of a potential role of Mn-ions would demand, e.g., operando electronic paramagnetic resonance, which, however, is beyond the scope of the present work.

With this notion, the $\chi(t)$-variation in the first 6 hours of charging ($0.9 \geq x > 0.53$) can be analyzed. A perfect fit of the experimental data is obtained with the assumption that $Co^{2+} \rightarrow Co^{3+}$ oxidation contributes by 10% to the charge compensation process and $Ni^{2+} \rightarrow Ni^{3+}$ by 90% within the first 6 h of charging (see black dashed line in Fig. 4.5c), which is in contrast to the exclusive Ni^{2+} oxidation obtained for $Li_xNi_{1/3}Mn_{1/3}Co_{1/3}O_2$. After 6 h of charging all Co^{2+}- and Ni^{2+}-ions are oxidized. The observed linear decrease of χ for charging times between $6\,\text{h} < t \leq 10\,\text{h}$ is consistent with an exclusive $Ni^{3+} \rightarrow Ni^{4+}$ (black dotted line in Fig. 4.5c).

The initial concentrations of the transition metal ions in the respective oxidation state as deduced from the magnetic susceptibility variation in Fig. 4.5c are summarized in Table 5.1b (denoted as proposed model). Taking into account these concentrations, a mean effective magnetic moment of $\overline{\mu}_{eff} = 2.72\mu_B$ is calculated (see Eq. (2.18) and Table 5.1b), which is in excellent agreement with the value $\overline{\mu}_{exp} = 2.71\mu_B$ obtained from the temperature-dependent ex-situ χ measurements of the initial state. From the required charge neutrality, an oxidation state of the oxygen ions of -1.88 is deduced,

which is equivalent to oxygen deficiency. Taking into account the ion concentrations obtained by ICP-MS analysis the initial state can be written as:

$$\mathrm{Li}^{+}_{0.9}\mathrm{Ni}^{2+}_{0.33}\mathrm{Ni}^{3+}_{0.25}\mathrm{Mn}^{4+}_{0.22}\mathrm{Co}^{2+}_{0.04}\mathrm{Co}^{3+}_{0.16}\mathrm{O}^{2-}_{1.88}. \tag{5.1}$$

In the subsequent discharging cycle (see Fig. 4.5), the variation of χ is correctly described by a reduction process occurring in the reversed order (including Co^{3+} reduction). It should be noted that the $Ni^{4+} \rightarrow Ni^{3+}$ reduction process of the first cycle is about 1000 s shorter (1000 s corresponds to $\Delta x = 1.7\,\%$ at a C/10-rate) than the prior oxidation process, which most likely reflects the well-known capacity loss [4,5]. The observed deviations of $\chi(t)$ from the $Ni^{4+} \rightarrow Ni^{3+}$ reduction at the beginning of the discharging cycle may indicate kinetic effects which are more relevant in the discharging cycle as it is the case for $Li_xNi_{1/3}Mn_{1/3}Co_{1/3}O_2$ [70]. These deviations can also be seen from Fig. 4.6 as slight hysteresis.

In summary, for both cathode materials the charge compensation processes upon battery charging can be divided into a sequence of two main steps. The first step is characterized by an exclusive $Ni^{2+} \rightarrow Ni^{3+}$ oxidation for $LiNi_{1/3}Mn_{1/3}Co_{1/3}O_2$ and by a simultaneous oxidation of Ni^{2+} and Co^{2+} for $Li_xNi_{0.6}Mn_{0.2}Co_{0.2}O_2$. Apart from the first oxidation step similarities have been found for both cathode material materials: (i) the first step proceeds until all Ni^{2+}-ions have been oxidized, (ii) the second step is characterized by an exclusive $Ni^{3+} \rightarrow Ni^{4+}$ oxidation and (iii) upon discharging the oxidation processes are fully reversible.

5.1.2 High-potential region (cut-off potentials 3.2 V and 4.8 V)

As outlined in the result section, the low Li concentration region can be studied by increasing the upper cut-off potential. Apart from the previous discussed oxidation processes, in Fig. 4.2 and Fig. 4.8 the straight lines according to Eq. (2.18) due to oxidation of $Co^{3+}(S = 0) \rightarrow Co^{4+}(S = 1/2)$ are also included as green lines for $Li_xNi_{1/3}Mn_{1/3}Co_{1/3}O_2$ and $Li_xNi_{0.6}Mn_{0.2}Co_{0.2}O_2$, respectively. For both cathode materials (see Fig. 4.2 and Fig. 4.8) these lines significantly deviate from the experimental observed χ-variations. Although, in the high potential region some charge is being lost due to electrolyte oxidation [70, 71] (the green-dashed lines in Fig. 4.2 and Fig. 4.8 account for this loss), this cannot explain the observed deviations. In the following discussion these deviations are addressed.

$\mathbf{Li_xNi_{1/3}Mn_{1/3}Co_{1/3}O_2}$

The χ-variations at the beginning of the 4$^{\text{th}}$ charging cycle ($40.5 > t > 47.8$ h) are in accordance with the variations described for the low potential region. Between $47.8 < t < 53$ h the observed gradual change of the susceptibility (see Fig. 4.2) indicates hat both Ni and Co are oxidized in this regime. The observed re-increase of χ during further charging (see $t > 53$ h in Fig. 4.2) is, in principle, consistent with the predicted oxidation $Co^{3+}(S = 0) \rightarrow Co^{4+}(S = 1/2)$[2]. As outlined at the beginning of this section, this linear χ-increase, however, is less pronounced as what is expected (green dashed-dotted line in Fig. 4.2). Apparently, the simple notion fails according to which only Co-ions are oxidized. As Ni^{4+} oxidation can be excluded and Mn^{4+}-ions are electrochemical inactive [23, 24, 26, 32, 33], a possible explanation is a contribution of O-ions to the charge compensation process as it is reported for $LiCoO_2$ [72, 79–83]. A simultaneous oxidation of Co and O in $Li_xNi_{1/3}Mn_{1/3}Co_{1/3}O_2$ for $x < 1/3$ was reported by Yoon *et al.* [33] and indirect evidence is deduced from in-situ XRD measurements [84] as well as from a reduced net magnetic moment per Co-ion found by theoretical calculations [30].

The proceeding increase of χ upon discharging shows that the Co oxidation process is irreversible. This notion is also supported by the capacity loss of 34% as evidenced by the reduced time of discharging (compare charging/discharging time). Therefore, instead of Co, Ni is reduced in the first step of discharging ($Ni^{4+} \rightarrow Ni^{3+}$). The less pronounced χ-increase compared to an exclusive Ni^{4+}-reduction (see black dotted line in Fig. 4.2) indicates a simultaneous reduction of both Ni- and O-ions. The observed linear χ-increase at the end of discharging $t > 66.9$ h is consistent with the exclusive reduction process of $Ni^{3+} \rightarrow Ni^{2+}$. Again, between the simultaneous reduction of both Ni- and O-ions and the exclusive $Ni^{3+} \rightarrow Ni^{2+}$ reduction a continuous transition rather than a sharp transition is observed.

$\mathbf{Li_xNi_{0.6}Mn_{0.2}Co_{0.2}O_2}$

For the measurements with the increased cut-off potential presented in Fig. 4.8 exactly the same $\chi(t)$ behavior was observed for the first 10 hours of charging as for the measurement presented in Fig. 4.5 demonstrating the reproducibility of the measurement. After 11.2 hours of charging, i.e., in the $Li_{x<0.21}Ni_{0.6}Mn_{0.2}Co_{0.2}O_2$ region, a re-increase of χ is observed. This re-increase is unexpected at this point of charging as a sufficient amount of Ni^{3+}-ions is still present. Actually, the Ni^{3+}-ions concentration

[2]Note: A re-increase during charging can only be explained by the oxidation of Co^{3+}, see Table 5.1a

is large enough such that the $Ni^{3+} \rightarrow Ni^{4+}$ oxidation process could continue until all Li-ions have been extracted from the cathode (see black dotted line in Fig. 4.8). Thus, before all Ni^{3+}-ions have been oxidized other ions are involved in the charge compensation process. According to Table 5.1b an increase of χ can only be explained by a $Co^{3+} \rightarrow Co^{4+}$ oxidation. Exclusive $Co^{3+} \rightarrow Co^{4+}$ oxidation can, however, be ruled out since the associated χ-increase would be to strong (see green solid line in Fig. 4.8). A reduced slope (displayed as dash-dotted line in Fig. 4.8) may indicate, on the one hand, that O-ions contribute to the charge compensation process as it was observed for $Li_xNi_{1/3}Mn_{1/3}Co_{1/3}O_2$ [72]. On the other hand, an ongoing oxidation of the remaining Ni^{3+} as well may reduce the $\chi(t)$-variation. The two processes cannot be distinguished by the magnetic measurements. In any case, $Co^{3+} \rightarrow Co^{4+}$ oxidation would contribute only by about 60% if a simultaneous oxidation of Co^{3+} and Ni^{3+}-ions is assumed and even less (by about 25%) in case of a simultaneous oxidation of Co^{3+}- and O-ions.

The subsequent discharging cycle shows that the processes occur in the reversed order. While for $Li_xNi_{1/3}Mn_{1/3}Co_{1/3}O_2$ the Co oxidation was found to be completely irreversible [72], in $Li_xNi_{0.6}Mn_{0.2}Co_{0.2}O_2$ this oxidation process is reversible, at least to a major extent as indicated by the $\chi(t)$ re-decrease which is in contrast to $Li_xNi_{1/3}Mn_{1/3}Co_{1/3}O_2$ (see Fig. 4.4). It should be noted, however, that the $Co^{4+} \rightarrow Co^{3+}$ reduction process is about 1.7 h shorter and also the $Ni^{4+} \rightarrow Ni^{3+}$ about 1.4 h shorter than the prior oxidation process. Thus, charging to high potentials accounts for ca. 19% capacity loss [3].

In summary, for both cathode materials the magnetic susceptibility in the high potential region re-increases again upon charging which is associated with the oxidation of Co^{3+}-ions. Nevertheless, from the observed χ-variation an exclusive Co oxidation can be ruled out. For $Li_xNi_{1/3}Mn_{1/3}Co_{1/3}O_2$ O-ions are identified to be involved in the charge compensation process. Also for $Li_xNi_{0.6}Mn_{0.2}Co_{0.2}O_2$ a contribution of O-ions could explain the observed χ-variations, however, in this case a contribution of Ni-ions cannot be excluded. In the subsequent discharging cycle the Co oxidation is irreversible for $Li_xNi_{1/3}Mn_{1/3}Co_{1/3}O_2$, in contrast to $Li_xNi_{0.6}Mn_{0.2}Co_{0.2}O_2$ where Co oxidation was found to be partial reversible.

[3] 19% capacity loss are equivalent to 3.1 h difference between charging and discharging

5.2 Charge compensation process in $Na_xV_2(PO_4)_3$

As vanadium is the only transition metal ion in this compound, the χ-variation is considered to arise from V^{3+}(S=1, $\mu = 2.83\mu_B$) $\rightarrow$ V^{4+}(S=1/2, $\mu = 1.73\mu_B$) oxidation/reduction during charging/discharging. The variation of the magnetic susceptibility as predicted according to Eq. (2.18) for pure vanadium oxidation/reduction is plotted as a function of charging time in Figs. 4.10 and 4.11b and d as black dashed line[4]. Apart from the first cycle the experimentally observed χ-variation can indeed be well described by the χ-variation expected for the V^{3+}/ V^{4+} oxidation/reduction. Deviations within the first cycle are only seen in the magnetic susceptibility data but not within the electrode potential (Fig. 4.10, 4.11a and c). Chemical side reactions at the surface of the electrode/electrolyte might be responsible for this deviations, similar to the reactions observed for some Li-ion battery cathode materials (see reviews [85, 86]). Upon such a reaction, Na-ions may be extracted from the cathode during charging but which do not contribute to battery charging. Since also the extraction of these Na^+-ions, not contributing to charging, gives rise to V-oxidation the χ-variation is stronger as compared to which is calculated using Faraday's law and the assumption that all charge carriers are used for charging (see lines in Fig. 4.11a). These side reaction processes might not be finished at the end of the charging cycle and, thus, also influences the magnetic measurements at the beginning of the first discharging cycle. After around 12 hours of battery operation (see Fig. 4.11a) the measured and predicted χ-variation according to Eq. (2.18) agree, indicating that the reaction not contributing to the battery cycling has vanished (i.e., is in equilibrium). The deviations at the beginning of the 25^{th} cycle in Fig. 4.11d may arise for the very same reason. The cell was under open circuit condition for 6 days before measured within the SQUID magnetometer. It is reasonable that the equilibrium conditions are different between potential and open circuit conditions.

[4]Due to the deviations within the first cycle $\Theta = 50\,\mathrm{K}$ in Eq. (2.18) was determined by ex-situ magnetic susceptibility measurement of a sample which was stopped in the 4^{th} charging cycle at a Na content of $x \approx 2.5$.

5.3 Charge-induced defects in $Li_xNi_{1/3}Mn_{1/3}Co_{1/3}O_2$

Although the variations of the positron lifetime are very small (Fig. 4.12), plotting all three measurements in one plot (see Fig. 5.2a) demonstrates that they are highly reproducible and, therefore, can be considered as very reliable. During battery charging Li-ions are extracted from the cathode material leaving behind vacancies. Although a very slow C/50-rate was chosen, the vacancy concentration on the Li sublattice reaches a concentration of 10^{-4} after 2 minutes of charging. As positron lifetime spectroscopy is sensitive to vacancy concentration between 10^{-7} and 10^{-4} [57] all positrons injected in the cathode material will quantitatively be captured by vacancies (saturation trapping occurs). Ex-situ measurements performed by P. Parz [87] confirmed saturation trapping even in the fully lithiated state. Only one lifetime component of 223 ps was observed which is attributed to Li-vacancies as it is significant higher than typical lifetime values in untrapped free states τ_f of other oxides, e.g. ZrO_2: $\tau_f \approx 174$ ps [88], MgO: $\tau_f \approx 152$ ps [88], TiO_2: $\tau_f \approx 148$ ps [89], Al_2O_3: $\tau_f \approx 140$ ps [88] or NiO: $\tau_f \approx 102$ ps [88]. Thus, in the region of saturation trapping any observed change in the positron lifetime (with the increasing amount of charging induced defects) is attributed to a change in open volume of the annihilation site due to vacancy clustering. In fact, for saturation trapping the mean positron lifetime represents a mean of the various lifetime components weighted by their respective concentrations (see chapter 2.1).

In the first sub-stage (I) most likely divacancies are formed in increasing amount upon charging as competing trap besides monovacancies (see Fig. 5.3). In sub-stage II the positron lifetime remains constant or even slightly decreases, which is unexpected as Li extraction prevails and, therefore, vacancies are continuously generated. In the very same Li concentration region in-situ XRD measurements revealed the coexistence of two structural phases [91]. The smaller unit–cell volume of the phase which forms in this region is presumably associated with a slight down-shift of the characteristic positron lifetime. It, therefore, appears obvious that this may mask a defect-induced τ-increase in this regime. This is schematically illustrated in Fig. 5.3. The reincrease of the positron lifetime for $x < 0.77$ is consistent with the end of the structural two phase region [91]. Any change in τ is thus again proportional to a change of the mean open volume size. Considering the high amount of vacancies present at this charging state, the τ-increase is attributed to a progressive amount of small vacancy agglomerates which are formed in addition to divacancies (sub-stage III in Fig. 5.3).

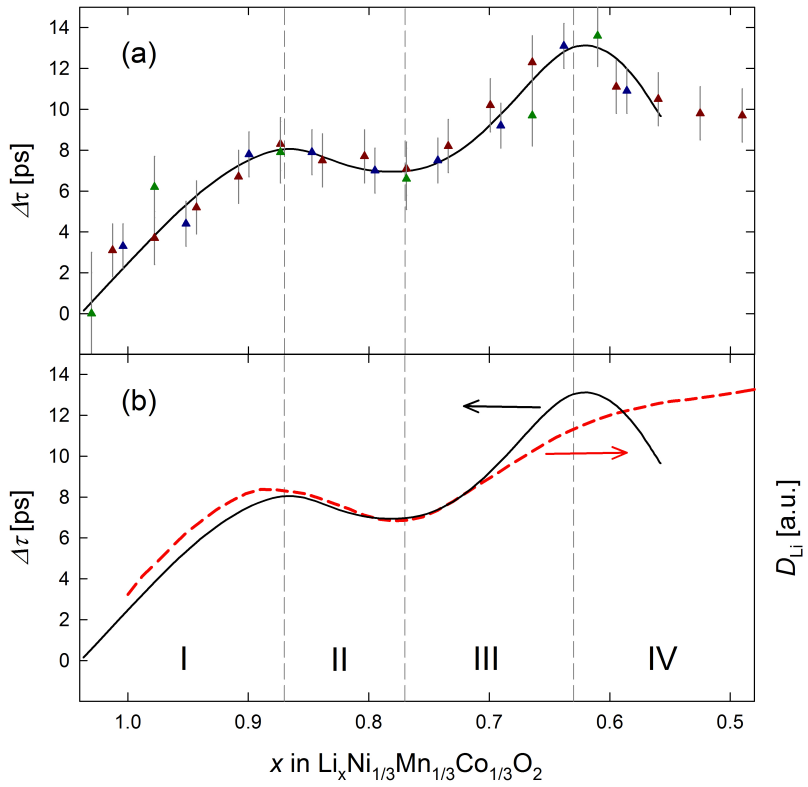

Figure 5.2: (a) Change in positron lifetime $\Delta\tau$ as a function of Li content x for the first charging cycle in $Li_xNi_{1/3}Mn_{1/3}Co_{1/3}O_2$ for the three independent measurements (Fig. 4.12(a)-(c)). (b) Comparison of $\Delta\tau$ and the numerical calculated Li diffusion coefficient D_{Li} (data for D_{Li} taken from Ref. [90]. The line in (a) is a guide for the eye and is redrawn in (b).

For $x < 0.63$ τ starts to decrease, which is remarkable as the vacancy concentration continuously increases upon charging. A structural phase transition like in sub-stage II can be excluded as origin for this behavior, since for $x < 0.63$ only one structural phase occurs [91]. Instead, a reordering of two-dimensional vacancy clusters to one-dimensional vacancy chains may give rise to a decrease of the positron lifetime as illustrated in Fig. 5.3. In fact, a vacancy reordering of this type was also found for $LiCoO_2$ by ex-situ positron lifetime measurements [20] in agreement with evidence from numerical simulations [92] and x-ray diffraction [11,12,14,93]. One may speculate whether also the similar τ-behavior in region II may be affected to a certain extend by vacancy reordering. In Li_xNiO_2, which is isostructural to $Li_xNi_{1/3}Mn_{1/3}Co_{1/3}O_2$, ordering processes for various Li contents have been reported [94].

During discharging the variation of the positron lifetime follows that of the charging cycle (see Fig. 4.12c1). Increasing the Li content (reducing the vacancy concentration)

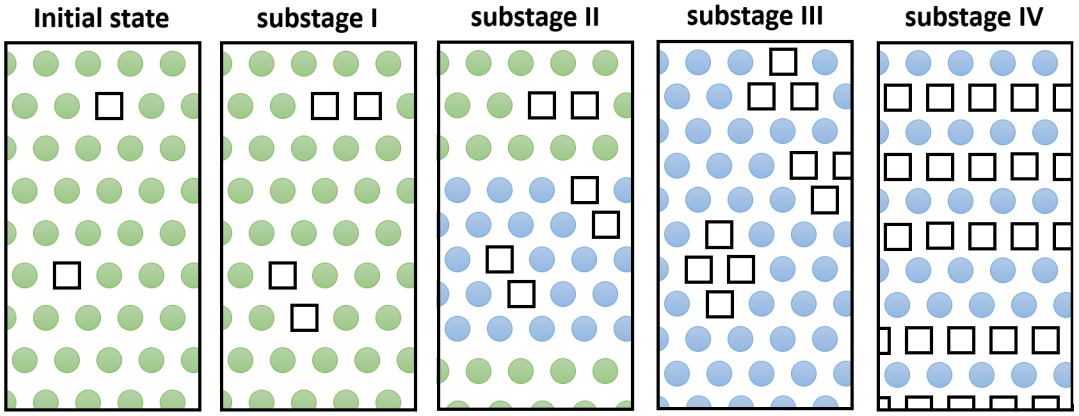

Figure 5.3: Illustration of the (001) Li-layer and the four sub-stages in the vacancy-induced defect formation process in $Li_xNi_{1/3}Mn_{1/3}Co_{1/3}O_2$ upon battery charging : Sub-stage I ($1 \geq x > 0.87$), substage II ($0.87 > x > 0.77$), substage III ($0.77 > x > 0.63$) and substage IV ($x < 0.63$). Note: Green and blue circles (both represent Li-ions) indicate different crystallographic phases.

results in an increase of τ for $x < 0.63$, followed by a decrease for $0.63 < x < 0.77$ and subsequently a slight increase again for $x > 0.77$. Note, that due to the high overpotential needed for Li insertion (see result section above) the discharging cycle was stopped at $x \approx 0.8$. However, within the monitored concentration region the positron lifetime variations is fully reversible (sub-stages IV to II).

Finally, the vacancy-type defects are compared with the Li-ion diffusivity. Figure 5.2b displays the variation of the change in positron lifetime as a function of Li content together with the diffusion coefficient numerical calculated by Wei et al. [90]. The variation of the vacancy-type defect pattern with Li content revealed by positron lifetime measurements nicely correlates with the respective variation of Li-diffusivity. For $x > 0.87$, both D_{Li} and $\Delta\tau$ increases, followed by a slight decrease for $0.87 > x > 0.77$ and a subsequent re-increase for $0.77 > x > 0.63$. It appears plausible that vacancy ordering in region IV affects the positron lifetime but not as much the diffusion coefficient which continues to increase in this regime, although with a reduced rate. Anyhow, these simulations clearly reveal that divacancies as detected here are a major vehicle of diffusion for $x \leq 0.8$ [90].

CHAPTER 6

Summary and Conclusion

In summary, within this thesis the charge compensation and defect evolution process of lithium ion and post lithium ion battery cathodes have been investigated. The charge compensation process was studied using a battery cell suitable for operando magnetic susceptibility measurements in a state-of-the-art SQUID magnetometer. Based on former battery cell studies at the Institute of Materials Physics, the battery cell design was further developed and optimized to enable a cycling efficiency of up to 98%, such that repetitive battery cycles can be studied. For investigating the defect evolution process the defect-sensitive technique of positron-electron annihilation was used. Therefore a battery cell with incorporated positron source was developed enabling for the first time the measurement of the positron lifetime under full electrochemical control. The major results are as follows:

Charge compensation process for $Li_xNi_{1/3}Mn_{1/3}Co_{1/3}O_2$ and $Li_xNi_{0.6}Mn_{0.2}Co_{0.2}O_2$

The measurements of both cathode materials revealed a linear variation of the magnetic susceptibility during battery charging and discharging from which a step-wise charge compensation process could be concluded. In the case of $Li_xNi_{1/3}Mn_{1/3}Co_{1/3}O_2$ at first exclusively Ni^{2+}-ions are being oxidized for Li contents $1 \geq x > 2/3$ followed by a sole oxidation of Ni^{3+} for $2/3 > x > 1/3$. After all Ni-ions have been oxidized to 4+ further battery charging results in a simultaneous oxidation of Co- and O-ions. For the iso-structural cathode material $Li_xNi_{0.6}Mn_{0.2}Co_{0.2}O_2$, the charge compensation process is more complex. Battery charging results first in the simultaneous oxidation $Ni^{2+} \rightarrow Ni^{3+}$ and $Co^{2+} \rightarrow Co^{3+}$ rather than the exclusive Ni^{3+} oxidation. After all Ni^{2+}- and Co^{2+}-ions have been oxidized (at $x = 0.53$), a sole oxidation process of $Ni^{3+} \rightarrow Ni^{4+}$ between $0.53 > x > 0.21$ occurs. Like for $Li_xNi_{1/3}Mn_{1/3}Co_{1/3}O_2$ from

the χ-variation upon further charging ($x < 0.21$) a simultaneous oxidation of Co and O-ions can be concluded. However, the Co oxidation process sets in before all Ni^{3+}-ions have been oxidized.

The charge compensation processes during the discharging cycle are dependent of the previous charging cycle. If the cut-off potential of the charging cycle was chosen to be 4.2 V the oxidation processes of the subsequent discharging (inserting of Li-ions) are fully reversible: For $Li_xNi_{1/3}Mn_{1/3}Co_{1/3}O_2$ first Ni^{4+} is reduced to Ni^{3+} followed by the reduction of Ni^{3+} to Ni^{2+} and in the case of $Li_xNi_{0.6}Mn_{0.2}Co_{0.2}O_2$ an exclusive reduction of Ni^{4+} followed by a simultaneous reduction of Ni^{3+} and Co^{3+}. In the charging regime with increased cut-off potential > 4.2 V, the reduction processes of the two cathode materials differ significantly. In the case of $Li_xNi_{1/3}Mn_{1/3}Co_{1/3}O_2$ the oxidized Co cannot be reduced anymore during the discharging cycle. Instead, discharging results first in a simultaneous reduction of Ni^{4+} and O-ions followed by sole $Ni^{3+} \rightarrow Ni^{2+}$ reduction. The irreversible Co oxidation gives rise to capacity loss of up to 30%. Also for the Ni-rich cathode material a capacity loss of 19% is observed after charging to higher voltages. Nevertheless, oxidized Co can again be reduced during battery discharging which is contrast to the iso-structural cathode material $Li_xNi_{1/3}Mn_{1/3}Co_{1/3}O_2$.

Charge compensation process for $Na_xV_2(PO_4)_3$

First operando SQUID measurements on the sodium ion cathode material $Na_xV_2(PO_4$ are presented. For this material the charge compensation process was confirmed to be entirely due to $V^{3+} \leftrightarrow V^{4+}$ oxidation/reduction during charging/discharging. However, during the first battery cycle the change in magnetic susceptibility indicates additional processes not contributing to battery charging.

Charging-induced defects in $Li_xNi_{1/3}Mn_{1/3}Co_{1/3}O_2$

For the defect evolution process during battery charging four different sub-stage could be identified. First an increase in the positron lifetime τ reflects an increasing amount of double vacancies for $x > 0.87$. After the initial increase τ slightly decreases between $0.87 > x > 0.77$ which is most likely caused by the co-existence of two structural phases. For Li contents $x < 0.77$, where only one structural phase is present, the observed τ-increase indicates vacancy clustering. Surprisingly, for Li contents below $x < 0.63$ the positron lifetime decreases although the number of vacancies continuously increases. A reduction of the positron lifetime can only be explained by vacancy reordering process, where the dimensionality of the defect is reduced. Due to the

layered structure of $Li_xNi_{1/3}Mn_{1/3}Co_{1/3}O_2$, vacancies are supposed to rearrange from 2-dimensional clusters into 1-dimensional chains. The observed vacancy formation processes are fully reversible during discharging.

Outlook

Due to the new cell design, rate-dependent magnetic susceptibility measurements became possible. Characterization of the oxidation/reduction process in dependence of the charging rate is of high interest for application relevant cathode materials. This in particular refers to battery cathodes used in electrical vehicles, where high charging rates are needed. Operando magnetic susceptibility studies of cathode materials with an even higher nickel content, like $Li_xNi_{0.8}Mn_{0.1}Co_{0.1}O_2$, are of high interest. Such measurements will have the potential to identify the various reversible and irreversible electrochemical processes, which can deliver valuable information for the optimization of these cathode materials. Moreover, the presented study of the Na-ion alternative has shown the potential of the electrochemical operando cell for post-Li-ion cathode materials. Thus, magnetic susceptibility measurements can give novel insights in the highly debated field of post-Li alternatives.

The developed operando cell for positron annihilation spectroscopy has opened up a new path for characterization of electrochemical processes. Besides of the very interesting study of the defect evolution process in different cathode materials, this cell design allows also for in-situ monitoring of defect formation in the wake of electrochemically induced dealloying, corrosion or intercalation processes.

Bibliography

[1] T. Ohzuku, A. Ueda. Why transition metal (di) oxides are the most attractive materials for batteries. *Solid State Ionics* **69** (1994) 201. doi:10.1016/0167-2738(94)90410-3

[2] M. Broussely, F. Perton, P. Biensan, J. Bodet, J. Labat, A. Lecerf, C. Delmas, A. Rougier, J. Pérès. Li_xNiO_2, a promising cathode for rechargeable lithium batteries. *J. Power Sources* **54** (1995) 109 . doi:10.1016/0378-7753(94)02049-9

[3] C. Delmas, M. Ménétrier, L. Croguennec, I. Saadoune, A. Rougier, C. Pouillerie, G. Prado, M. Grüne, L. Fournès. An overview of the Li(Ni,M)O2 systems: syntheses, structures and properties. *Electrochim. Acta* **45** (1999) 243. doi:10.1016/S0013-4686(99)00208-X

[4] X. Zeng, G.-L. Xu, Y. Li, X. Luo, F. Maglia, C. Bauer, S. F. Lux, O. Paschos, S.-J. Kim, P. Lamp, J. Lu, K. Amine, Z. Chen. Kinetic Study of Parasitic Reactions in Lithium-Ion Batteries: A Case Study on $LiNi_{0.6}Mn_{0.2}Co_{0.2}O_2$. *ACS Appl. Mater. Inter.* **8** (2016) 3446. doi:10.1021/acsami.5b11800. PMID: 26795232

[5] H. Cao, Y. Zhang, J. Zhang, B. Xia. Synthesis and electrochemical characteristics of layered $LiNi_{0.6}Co_{0.2}Mn_{0.2}O_2$ cathode material for lithium ion batteries. *Solid State Ionics* **176** (2005) 1207 . doi:10.1016/j.ssi.2005.02.023

[6] J.-M. Tarascon. Is lithium the new gold? *Nat. Chem.* **2** (2010) 510. doi:10.1038/nchem.680

[7] H. Kim, H. Kim, Z. Ding, M. H. Lee, K. Lim, G. Yoon, K. Kang. Recent Progress in Electrode Materials for Sodium-Ion Batteries. *Adv. Energy Mater.* **6** (2016) 1600943.
doi:10.1002/aenm.201600943

[8] C. Fang, Y. Huang, W. Zhang, J. Han, Z. Deng, Y. Cao, H. Yang. Routes to High Energy Cathodes of Sodium-Ion Batteries. *Adv. Energy Mater.* **6** (2015) 1501727.
doi:10.1002/aenm.201501727

[9] H. Pan, Y.-S. Hu, L. Chen. Room-temperature stationary sodium-ion batteries for large-scale electric energy storage. *Energy Environ. Sci.* **6** (2013) 2338.
doi:10.1039/C3EE40847G

[10] R. Chebiam, A. Kannan, F. Prado, A. Manthiram. Comparison of the chemical stability of the high energy density cathodes of lithium-ion batteries. *Electrochem. Commun.* **3** (2001) 624.
doi:10.1016/S1388-2481(01)00232-6

[11] G. G. Amatucci, J. M. Tarascon, L. C. Klein. CoO_2, The End Member of the Li_xCoO_2 Solid Solution. *J. Electrochem. Soc.* **143** (1996) 1114.
doi:10.1149/1.1836594

[12] J. N. Reimers, J. R. Dahn. Electrochemical and In Situ X-Ray Diffraction Studies of Lithium Intercalation in Li_xCoO_2. *J. Electrochem. Soc.* **139** (1992) 2091.
doi:10.1149/1.2221184

[13] J.-S. Hong, J. R. Selman. Relationship Between Calorimetric and Structural Characteristics of Lithium-Ion Cells I. Thermal Analysis and Phase Diagram. *J. Electrochem. Soc.* **147** (2000) 3183.
doi:10.1149/1.1393881

[14] Y. Shao-Horn, S. Levasseur, F. Weill, C. Delmas. Probing Lithium and Vacancy Ordering in O3 Layered Li_xCoO_2 ($x \approx 0.5$): An Electron Diffraction Study. *J. Electrochem. Soc.* **150** (2003) A366.
doi:10.1149/1.1553787

[15] S. Laubach, S. Laubach, P. C. Schmidt, D. Ensling, S. Schmid, W. Jaegermann, A. T. en, K. Nikolowskid, H. Ehrenberge. Changes in the crystal and electronic structure of $LiCoO_2$ and $LiNiO_2$ upon Li intercalation and de-intercalation. *Phys. Chem. Chem. Phys.* **11** (2009) 3278. doi:10.1039/B901200A

[16] S. F. Amalraj, D. Aurbach. The use of in situ techniques in R&D of Li and Mg rechargeable batteries. *J. Solid State Electrochem.* **15** (2011) 877. doi:10.1007/s10008-011-1324-9

[17] S. Ramdon, B. Bhushan, S. C. Nagpure. In situ electrochemical studies of lithium-ion battery cathodes using atomic force microscopy. *J. Power Sources* **249** (2014) 373. doi:10.1016/j.jpowsour.2013.10.099

[18] P. P. R. M. L. Harks, F. M. Mulder, P. H. L. Notten. In situ methods for Li-ion battery research: A review of recent developments. *J. Power Sources* **288** (2015) 92. doi:10.1016/j.jpowsour.2015.04.084

[19] S. Topolovec, H. Krenn, R. Würschum. Electrochemical cell for in-situ electrodeposition of magnetic thin films in a superconducting quantum interference device magnetometer. *Rev. Sci. Instrum.* **86** (2015) 063903. doi:10.1063/1.4922462

[20] P. Parz, B. Fuchsbichler, S. Koller, B. Bitschnau, F.-A. Mautner, W. Puff, R. Würschum. Charging-induced defect formation in Li_xCoO_2 battery cathodes studied by positron annihilation spectroscopy. *Appl. Phys. Lett.* **102** (2013) 151901. doi:10.1063/1.4801998

[21] S. Seidlmayer, I. Buchberger, M. Reiner, T. Gigl, R. Gilles, H. A. Gasteiger, C. Hugenschmidt. First-cycle defect evolution of $Li_{1-x}Co_{1/3}Ni_{1/3}Mn_{1/3}O_2$ lithium ion battery electrodes investigated by positron annihilation spectroscopy. *J. Power Sources* **336** (2016) 224. doi:10.1016/j.jpowsour.2016.10.050

[22] K. Shaju, G. S. Rao, B. Chowdari. Performance of layered $Li(Ni_{1/3}Co_{1/3}Mn_{1/3})O_2$ as cathode for Li-ion batteries. *Electrochim. Acta* **48** (2002) 145.
doi:10.1016/S0013-4686(02)00593-5

[23] C. F. Petersburg, Z. Li, N. A. Chernova, M. S. Whittingham, F. M. Alamgir. Oxygen and transition metal involvement in the charge compensation mechanism of $LiNi_{1/3}Mn_{1/3}Co_{1/3}O_2$ cathodes. *J. Mater. Chem.* **22** (2012) 19993.
doi:10.1039/C2JM33392A

[24] J.-M. Kim, H.-T. Chung. The first cycle characteristics of $Li[Ni_{1/3}Co_{1/3}Mn_{1/3}]O_2$ charged up to 4.7 V. *Electrochim. Acta* **49** (2004) 937.
doi:10.1016/j.electacta.2003.10.005

[25] Y. W. Tsai, B. J. Hwang, G. Ceder, H. S. Sheu, D. G. Liu, J. F. Lee. In-Situ X-ray Absorption Spectroscopic Study on Variation of Electronic Transitions and Local Structure of $LiN_{1/3}Co_{1/3}Mn_{1/3}O_2$ Cathode Material during Electrochemical Cycling. *Chem. Mater.* **17** (2005) 3191.
doi:10.1021/cm048027v

[26] A. Deb, U. Bergmann, S. P. Cramer, E. J. Cairns. In situ x-ray absorption spectroscopic study of the $Li[Ni_{1/3}Co_{1/3}Mn_{1/3}]O_2$ cathode material. *J. Appl. Phys.* **97** (2005) 113523.
doi:10.1063/1.1921328

[27] M. G. Kim, H. J. Shin, J.-H. Kim, S.-H. Park, Y.-K. Sun. XAS Investigation of Inhomogeneous Metal-Oxygen Bond Covalency in Bulk and Surface for Charge Compensation in Li-Ion Battery Cathode Li $[Ni_{1/3}Co_{1/3}Mn_{1/3}]O_2$ Material. *J. Electrochem. Soc.* **152** (2005) A1320.
doi:10.1149/1.1926647

[28] H. Kobayashi, Y. Arachi, S. Emura, H. Kageyama, K. Tatsumi, T. Kamiyama. Investigation on lithium de-intercalation mechanism for $Li1_{1-y}Ni_{1/3}Mn_{1/3}Co_{1/3}O_2$. *J. Power Sources* **146** (2005) 640.
doi:110.1016/j.jpowsour.2005.03.081

[29] X. Liu, D. Wang, G. Liu, V. Srinivasan, Z. Liu, Z. Hussain, W. Yang. Distinct charge dynamics in battery electrodes revealed by in situ and operando soft X-ray spectroscopy. *Nat. Commun.* **4** (2013) 2568.
doi:10.1038/ncomms3568

[30] B. J. Hwang, Y. W. Tsa, D. Carlier, G. Ceder. A Combined Computational/Experimental Study on $LiNi_{1/3}Co_{1/3}Mn_{1/3}O_2$. *Chem. Mater.* **15** (2003) 3676.
doi:10.1021/cm030299v

[31] Z. Li, N. A. Chernova, M. Roppolo, S. Upreti, C. Petersburg, F. M. Alamgir, M. S. Whittingham. Comparative Study of the Capacity and Rate Capability of $LiNi_yMn_yCo_{1-2y}O_2$(y=0.5, 0.45, 0.4, 0.33). *J. Electrochem. Soc.* **158** (2011) A516.
doi:10.1149/1.3562212

[32] W.-S. Yoon, M. Balasubramanian, K. Y. Chung, X.-Q. Yang, J. McBreen, C. P. Grey, D. A. Fischer. Investigation of the Charge Compensation Mechanism on the Electrochemically Li-Ion Deintercalated $Li_{1-x}Co_{1/3}Ni_{1/3}Mn_{1/3}O_2$ Electrode System by Combination of Soft and Hard X-ray Absorption Spectroscopy. *J. Am. Chem. Soc.* **127** (2005) 17479.
doi:10.1021/ja0530568

[33] W.-S. Yoon, C. P. Grey, M. Balasubramanian, X.-Q. Yang, D. A. Fischer, J. McBreen. Combined NMR and XAS Study on Local Environments and Electronic Structures of Electrochemically Li-Ion Deintercalated $Li_{1-x}N_{1/3}Mn_{1/3}Co_{1/3}O_2$ Electrode System. *Electrochem. Solid State* **7** (2004) A53.
doi:10.1149/1.1643592

[34] A. Mauger, F. Gendron, C. Julien. Magnetic properties of $Li_xNi_yMn_yCo_{1-2y}O_2$ ($0.2 \leq 1-2y \leq 0.5, 0 \leq x \leq 1$). *J. Alloy. Compd.* **520** (2012) 42.
doi:10.1016/j.jallcom.2011.12.055

[35] E. Shinova, R. Stoyanova, E. Zhecheva, G. Ortiz, P. Lavela, J. Tirado. Cationic distribution and electrochemical performance of $LiCo_{1/3}Ni_{1/3}Mn_{1/3}O_2$ electrodes for lithium-ion batteries. *Solid State Ionics* **179** (2008) 2198. doi:10.1016/j.ssi.2008.07.026

[36] M. Labrini, I. Saadoune, F. Scheiba, A. Almaggoussi, J. Elhaskouri, P. Amoros, H. Ehrenberg, J. Brötz. Magnetic and structural approach for understanding the electrochemical behavior of $LiNi_{0.33}Co_{0.33}Mn_{0.33}O_2$ positive electrode material. *Electrochim. Acta* **111** (2013) 567. doi:10.1016/j.electacta.2013.08.051

[37] S. Miao, M. Kocher, P. Rez, B. Fultz, Y. Ozawa, R. Yazami, C. C. Ahn. Local Electronic Structure of Layered $Li_xNi_{0.5}Mn_{0.5}O_2$ and $Li_xNi_{1/3}Mn_{1/3}Co_{1/3}O_2$. *J. Phys. Chem. B* **109** (2005) 23473. doi:10.1021/jp0542266

[38] Y. Koyama, I. Tanaka, H. Adachi, Y. Makimura, T. Ohzuku. Crystal and electronic structures of superstructural $Li_{1-x}[Co_{1/3}Ni_{1/3}Mn_{1/3}]O_2$ ($0 \geq x \geq 1$). *J. Power Sources* **119-121** (2003) 644. doi:10.1016/S0378-7753(03)00194-0

[39] D. Mohanty, H. Gabrisch. Microstructural investigation of $Li_xN_{1/3}Mn_{1/3}Co_{1/3}O_2$ ($x \leq 1$) and its aged products via magnetic and diffraction study. *J. Power Sources* **220** (2012) 405. doi:10.1016/j.jpowsour.2012.08.005

[40] G. Klinser, S. Topolovec, H. Kren, S. Koller, H. Krenn, R. Würschum. Charging of lithium cobalt oxide battery cathodes studied by means of magnetometry. *Solid State Ionics* **293** (2016) 64. doi:10.1016/j.ssi.2016.06.004

[41] S. Topolovec. *In-situ studies of the correlations between electrochemical processes and magnetic properties.* PhD thesis, Graz University of Technology, 2015

[42] F. Schipper, M. Dixit, D. Kovacheva, M. Talianker, O. Haik, J. Grinblat, E. M. Erickson, C. Ghanty, D. T. Major, B. Markovsky, D. Aurbach. Stabilizing nickel-rich layered cathode materials by a high-charge cation doping strategy: zirconium-doped $LiNi_{0.6}Co_{0.2}Mn_{0.2}O_2$. *J. Mater. Chem. A* **4** (2016) 16073.
doi:10.1039/C6TA06740A

[43] H. Sun, K. Zhao. Electronic Structure and Comparative Properties of $LiNi_xMn_yCo_zO_2$ Cathode Materials. *J. Phys. Chem. C* **121** (2017) 6002

[44] N. Kosova, E. Devyatkina, V. Kaichev. Optimization of Ni^{2+}/Ni^{3+} ratio in layered Li(Ni,Mn,Co)O_2 cathodes for better electrochemistry. *J. Power Sources* **174** (2007) 965.
doi:10.1016/j.jpowsour.2007.06.051

[45] R. Krause-Rehbberg, H. Leipner. *Positron Annihilation in Semiconductors; Defect Studies*. Springer-Verlag, 1999

[46] P. Hautojärvi, A. Vehanen. *Topics in Current Physics: Positrons in Solids*. Springer-Verlag, 1979

[47] H. Lueken. *Magnetochemie*. B.G. Teubner Stuttgart, 1999.
doi:10.1007/978-3-322-80118-0

[48] P. Dirac. The quantum theory of the electron. *Proceedings of the Royal Society of London A: Mathematical, Physical and Engineering Sciences* **117** (1928) 610.
doi:10.1098/rspa.1928.0023

[49] C. D. Anderson. The Positive Electron. *Phys. Rev.* **43** (1933) 491.
doi:10.1103/PhysRev.43.491

[50] I. K. MacKenzie, T. L. Khoo, A. B. McDonald, B. T. A. McKee. Temperature Dependence of Positron Mean Lives in Metals. *Phys. Rev. Lett.* **19** (1967) 946.
doi:10.1103/PhysRevLett.19.946

[51] T. Hyodo, T. McMullen, A. T. Stewart. Positron motion in metals. II. Models for data analysis. *Can. J. Phys.* **62** (1984) 297.
doi:10.1139/p84-045

[52] A. Perkins, J. P. Carbotte. Effect of the Positron-Phonon Interaction on Positron Motion. *Phys. Rev. B* **1** (1970) 101. doi:10.1103/PhysRevB.1.101

[53] W. Brandt, R. Paulin. Positron implantation-profile effects in solids. *Phys. Rev. B* **15** (1977) 2511. doi:10.1103/PhysRevB.15.2511

[54] M. J. Puska, R. M. Nieminen. Theory of positrons in solids and on solid surfaces. *Rev. Mod. Phys.* **66** (1994) 841. doi:10.1103/RevModPhys.66.841

[55] H. Schaefer. Investigation of Thermal Equilibrium Vacancies in Metals by Positron Annihilation. *physi. stat. sol. (a)* **102** (1987) 47. doi:10.1002/pssa.2211020104

[56] R. West. Positron studies of condensed matter. *Adv. Phys.* **22** (1973) 263. doi:10.1080/00018737300101299

[57] U. Brossmann, W. Puff, R. Würschum. *In Characterization of Materials*, Chapter: Positron Annihilation Studies of Materials. American Cancer Society, 2003. doi:10.1002/0471266965.com110

[58] R. C. Black, F. C. Wellstood. *The SQUID Handbook Vol II: Applications of SQUIDs and SQUID Systems*, Chapter: Measurements of Magnetism and Magnetic Properties of Matter. Wiley-VCH, 2006

[59] T. Traussnig. *Charge-induced property tuning of nanoscaled metals and metal oxides*. PhD thesis, Graz University of Technology, 2011

[60] M. Stückler. *Optimierung von Lithium-Sekundärzellen für operando SQUID-Magnetometrie von Li[Ni,Mn,Co]-Oxid Batteriekathoden*. Master thesis, Graz University of Technology, 2017

[61] M. Dahbi, J. M. Wikberg, I. Saadoune, T. Gustafsson, P. Svedlindh, K. Edström. Electrochemical behavior of $LiNi_{1-y-z}Co_yMn_zO_2$ probed through structural and magnetic properties. *J. Appl. Phys.* **111** (2012) 023904. doi:10.1063/1.3676434

[62] N. Kizilitas-Yavuz, M. Herklotz, A. M. Hashem, H. M. Abuzeid, B. Schwarz, H. Ehrenberg, A. Mauger, C. M. Julien. Synthesis, structural, magnetic and electrochemical properties of $LiNi_{1/3}Mn_{1/3}Co_{1/3}O_2$ prepared by a sol-gel method using table sugar as chelating agent. *Electrochim. Acta* **113** (2013) 313.
doi:10.1016/j.electacta.2013.09.065

[63] C. Huang, D. Chen, Y. Huang, Y. Guo. Sol–gel synthesis of $Li_3V_2(PO_4)_3$/C cathode materials with high electrical conductivity. *Electrochim. Acta* **100** (2013) 1.
doi:10.1016/j.electacta.2013.03.073

[64] G. Klinser. *Charakterisierung des Beladungszustandes von Lithium-Kobaltoxid Batteriekathoden durch Magnetometrie.* Master thesis, Graz University of Technology, 2014

[65] P. Kirkegaard, J. V. Olsen, M. Eldrup, N. J. Pedersen. *PALSfit3: A software package for analysing positron lifetime spectra.* Kgs. Lyngby: Technical University of Denmark (DTU), 2017

[66] M. Leitner. *Synthesis and Positron Annihilation Lifetime Spectroscopy of Nanoporous Platinum.* Master thesis, Graz University of Technology, 2015

[67] A. K. M. Kostrzewa, G. Bujnarowski, M. Szuszkiewicz. Positron Lifetime in Hostaphan. *Proceedings of the 36th Polish Seminar on Positron Annihilation* **110** (2006) 615.
doi:10.12693/APhysPolA.110.615

[68] N. Djourelov, M. Misheva. Source correction in positron annihilation lifetime spectroscopy. *J. Phys.: Condens. Matter* **8** (1996) 2081.

[69] S. McGuire, D. J. Keeble. Positron lifetimes of polycrystalline metals: A positron source correction study. *J. Appl. Phys.* **100** (2006) 103504.
doi:10.1063/1.2384794

[70] J. Kasnatscheew, M. Evertz, B. Streipert, R. Wagner, R. Klopsch, B. Vortmann, H. Hahn, S. Nowak, M. Amereller, A.-C. Gentschev, P. Lamp, M. Winter. The truth about the 1st cycle Coulombic efficiency of $LiNi_{1/3}Co_{1/3}Mn_{1/3}O_2$ (NCM) cathodes. *Phys. Chem. Chem. Phys.* **18** (2016) 3956.
doi:10.1039/C5CP07718D

[71] B. B. Berkes, A. Jozwiuk, H. Sommer, T. Brezesinski, J. Janek. Simultaneous acquisition of differential electrochemical mass spectrometry and infrared spectroscopy data for in situ characterization of gas evolution reactions in lithium-ion batteries. *Electrochem. Commun.* **60** (2015) 64 .
doi:10.1016/j.elecom.2015.08.002

[72] G. Klinser, S. Topolovec, H. Kren, S. Koller, W. Goessler, H. Krenn, R. Würschum. Continuous monitoring of the bulk oxidation states in $Li_xNi_{1/3}Mn_{1/3}Co_{1/3}O_2$ during charging and discharging. *Appl. Phys. Lett* **109** (2016) 213901.
doi:10.1063/1.4968547

[73] I. Saadoune, M. Dahbi, M. Wikberg, T. Gustafsson, P. Svedlindh, K. Edström. Effect of the synthesis temperature on the structure and electrochemical behaviour of the $LiNi_{0.65}Co_{0.25}Mn{-}0.1O_2$ positive electrode material. *Solid State Ionics* **178** (2008) 1668.
doi:10.1016/j.ssi.2007.10.019

[74] H. M. Hollmark, L.-C. Duda, M. Dahbi, I. Saadoune, T. Gustafsson, K. Edström. Resonant Soft X-Ray Emission Spectroscopy and X-Ray Absorption Spectroscopy on the Cathode Material $LiN_{0.65}Co_{0.25}Mn_{0.1}O_2$. *J. Electrochem. Soc.* **157** (2010) A962.
doi:10.1149/1.3454739

[75] N. V. Kosova, E. T. Devyatkina, V. V. Kaichev, D. G. Kellerman. Effect of electronic state of ions on the electrochemical properties of layered cathode materials $LiNi_{1-2x}Co_xMn_xO_2$. *Russ. J. Electrochem.* **44** (2008) 543.
doi:10.1134/S1023193508050066

[76] D. Kim, J.-M. Lim, Y.-G. Lim, J.-S. Yu, M.-S. Park, M. Cho, K. Cho. Design of Nickel-rich Layered Oxides Using d Electronic Donor for Redox Reactions. *Chem. Mater.* **27** (2015) 6450.
doi:10.1021/acs.chemmater.5b02697

[77] A. Niemöller, P. Jakes, S. Eurich, A. Paulus, H. Kungl, R.-A. Eichel, J. Granwehr. Monitoring local redox processes in $LiNi_{0.5}Mn_{1.5}O_4$ battery cathode material by in operando EPR spectroscopy. *J. Chem. Phys.* **148** (2018) 014705.
doi:10.1063/1.5008251

[78] W. Kläui, W. Eberspach, P. Gütlich. Spin-crossover cobalt(III) complexes: steric and electronic control of spin state. *Inorg. Chem.* **26** (1987) 3977.
doi:10.1021/ic00271a004

[79] D. Kellerman, V. Galakhov, A. Semenova, Y. Blinovskov, O. Leonidova. Semiconductor-metal transition in defect lithium cobaltite. *Phys. Solid State* **48** (2006) 548.
doi:10.1134/S106378340603022X

[80] C.-H. Chen, B.-J. Hwang, C.-Y. Chen, S.-K. Hu, J.-M. Chen, H.-S. Sheu, J.-F. Lee. Soft X-ray absorption spectroscopy studies on the chemically delithiated commercial $LiCoO_2$ cathode material. *J. Power Sources* **174** (2007) 938.
doi:10.1016/j.jpowsour.2007.06.083

[81] W.-S. Yoon, K.-B. Kim, M.-G. Kim, M.-K. Lee, H.-J. Shin, J.-M. Lee, J.-S. Lee, C.-H. Yo. Oxygen Contribution on Li-Ion Intercalation–Deintercalation in $LiCoO_2$ Investigated by O K-Edge and Co L-Edge X-ray Absorption Spectroscopy. *J. Phys. Chem. B* **106** (2002) 2526.
doi:10.1021/jp013735e

[82] L. Dahéron, R. Dedryvére, H. Martinez, M. Ménétrier, C. Denage, C. Delmas, D. Gonbeau. Electron Transfer Mechanisms upon Lithium Deintercalation from $LiCoO_2$ to CoO_2 Investigated by XPS. *Chem. Mater.* **20** (2008) 583.
doi:10.1021/cm702546s

[83] S. Topolovec, H. Kren, G. Klinser, S. Koller, H. Krenn, R. Würschum. Operando magnetometry on Li_xCoO_2 during charging/discharging. *J. Solid State Electrochem.* **20** (2016) 1491.
doi:10.1007/s10008-015-3110-6

[84] K. Ishidzu, Y. Oka, T. Nakamura. Lattice volume change during charge/discharge reaction and cycle performance of $Li[Ni_xCo_yMn_z]O_2$. *Solid State Ionics* **288** (2016) 176.
doi:10.1016/j.ssi.2016.01.009

[85] P. Arora, R. E. White, M. Doyle. Capacity Fade Mechanisms and Side Reactions in Lithium-Ion Batteries. *J. Electrochem. Soc.* **145** (1998) 3647.
doi:10.1149/1.1838857

[86] V. Etacheri, R. Marom, R. Elazari, G. Salitra, D. Aurbach. Challenges in the development of advanced Li-ion batteries: a review. *Energy Environ. Sci.* **4** (2011) 3243.
doi:10.1039/C1EE01598B

[87] P. Parz. *Vacancy-type and interface related defects in ultra-fine grained alloys and oxides.* PhD thesis, Graz University of Technology, 2013

[88] H.-E. Schaefer, M. Forster. As-grown metal oxides and electron-irradiated Al_2O_3 studied by positron lifetime measurements. *Mater. Sci. Eng. A* **109** (1989) 161.
doi:10.1016/0921-5093(89)90581-9

[89] A. A. Valeeva, A. A. Rempel, W. Sprengel, H.-E. Schaefer. Identification and study of vacancies in titanium monoxide by means of positron annihilation techniques. *Phys. Chem. Chem. Phys.* **5** (2003) 2304.
doi:10.1039/B300147B

[90] Y. Wei, J. Zheng, S. Cui, X. Song, Y. Su, W. Deng, Z. Wu, X. Wang, W. Wang, M. Rao, Y. Lin, C. Wang, K. Amine, F. Pan. Kinetics Tuning of Li-Ion Diffusion in Layered $Li(Ni_xMn_yCo_z)O_2$. *J. Am. Chem. Soc.* **137** (2015) 8364.
doi:10.1021/jacs.5b04040

[91] W.-S. Yoon, K. Y. Chung, J. McBreen, X.-Q. Yang. A comparative study on structural changes of $LiCo_{1/3}Ni_{1/3}Mn_{1/3}O_2$ and $LiNi_{0.8}Co_{0.15}Al_{0.05}O_2$ during first charge using in situ XRD. *Electrochem. Commun.* **8** (2006) 1257. doi:10.1016/j.elecom.2006.06.005

[92] A. Van der Ven, M. K. Aydinol, G. Ceder, G. Kresse, J. Hafner. First-principles investigation of phase stability in Li_xCoO_2. *Phys. Rev. B* **58** (1998) 2975. doi:10.1103/PhysRevB.58.2975

[93] J. N. Reimers, J. R. Dahn, U. von Sacken. Effects of Impurities on the Electrochemical Properties of $LiCoO_2$. *J. Electrochem. Soc.* **140** (1993) 2752. doi:10.1149/1.2220905

[94] M. E. Arroyo y de Dompablo, A. Van der Ven, G. Ceder. First-principles calculations of lithium ordering and phase stability on Li_xNiO_2. *Phys. Rev. B* **66** (2002) 064112. doi:10.1103/PhysRevB.66.064112

Acknowledgments

I would like to express my special thanks to the following persons for their contribution to the success of this thesis and also for their support during the last years:

Univ.-Prof. Dr. Roland Würschum, Institute of Materials Physics, TU Graz
For given me the opportunity to work on this thesis, the valuable supervision and guidance as well as the pleasant and respectful working atmosphere throughout the past years. I am especially grateful for the productive discussions and support during the writing process of this thesis as well as the published articles.

Univ.-Prof. Dr. Heinz Krenn, Institute of Physics, KFU Graz
For given me the opportunity to perform the SQUID magnetometry measurements at his laborotory, his support during these measurements and their fruitful discussions.

Univ.-Prof. Dr. Andreas Ney, Institute of Semiconductor & Solid State Physics, JKU Linz
For accepting to act as an external reviewer for this thesis and for his valuable comments during the preliminary evaluation.

Assoc.Prof. Dr. Wolfgang Sprengel, Institute of Materials Physics, TU Graz
For the excellent experimental support regarding positron spectroscopy and the valuable discussion of the obtained results.

Dr. Harald Kren, Dr. Stefan Koller and Christian Baumann, VARTA Micro Innovation GmbH, Graz
For their collaboration on the Li-ion battery studies. In particular, Christian Baumann for preparing the samples for the magnetic ex-situ measurements.

Dr. Ilie Hanzu, Dr. Denise Tapler and Dipl.-Ing. Roman Zettl, Institute for Chemistry and Technology of Materials, TU Graz
For their collaboration on the Na-ion battery study. In particular, for synthesis of the cathode material, electrolyte preparation and preparing samples for the magnetic ex-situ measurements.

Dipl.-Ing. Martin Stückler, formerly Institute of Materials Physics, TU Graz
For his productive collaboration on the development of the SQUID operando cell as well as first magnetic studies on $Li_xNi_{0.6}Mn_{0.2}Co_{0.2}O_2$.

Dr. Stefan Topolovec, formerly Institute of Materials Physics, TU Graz
For sharing the experience on the operando battery cell for a SQUID magnetometer which served as a base for the new developed cell.

Dipl.-Ing. Laura Resch, Institute of Materials Physics, TU Graz
For the excellent collaboration and discussion of positron measurements of the Al alloy AW6060 (not presented in this thesis).

Dr. Martin Luckabauer, formerly Institute of Materials Physics, TU Graz
For his productive collaboration and giving the impetus on the aging measurements on Al alloys (not presented in this thesis).

Ao.Univ.-Prof. Dr. Walter Goessler, Institute of Chemistry, KFU Graz
For performing the ICP-MS analysis on the Li-ion cathode materials.

All present and former colleagues of the Institute of Materials Physics
For the excellent working atmosphere, their help during experimental studies and fruitful discussion during the last years.

My family and friends
For their encouragement during the last years, which helped me to reach my goals. In particular, I want to thank my parents Barbara and Anton, my sister Antonia and my girlfriend Maria for their tremendous support, their love and good times spent together.

AFFIDAVIT

I declare that I have authored this thesis independently, that I have not used other than the declared sources/resources, and that I have explicitly indicated all material which has been quoted either literally or by content from the sources used. The text document uploaded to TUGRAZonline is identical to the present doctoral thesis.

Date

Signature